


InSight Auxiliary Payload Sensor Suite (APSS)

D. Banfield¹  · J.A. Rodriguez-Manfredi² · C.T. Russell³ · K.M. Rowe³ ·
D. Leneman³ · H.R. Lai³ · P.R. Cruce³ · J.D. Means³ · C.L. Johnson^{4,5} · A. Mittelholz⁴ ·
S.P. Joy³ · P.J. Chi³ · I.G. Mikellides⁶ · S. Carpenter⁷ · S. Navarro² · E. Sebastian² ·
J. Gomez-Elvira² · J. Torres² · L. Mora² · V. Peinado² · A. Lepinette² ·
The TWINS Team² · K. Hurst⁶ · P. Lognonné⁸ · S.E. Smrekar⁶ · W.B. Banerdt⁶

Received: 2 July 2018 / Accepted: 3 December 2018
© Springer Nature B.V. 2018

Abstract NASA's InSight mission to Mars will measure seismic signals to determine the planet's interior structure. These highly sensitive seismometers are susceptible to corruption of their measurements by environmental changes. Magnetic fields, atmosphere pressure changes, and local winds can all induce apparent changes in the seismic records that are not due to propagating ground motions. Thus, InSight carries a set of sensors called the Auxiliary Payload Sensor Suite (APSS) which includes a magnetometer, an atmospheric pressure sensor, and a pair of wind and air temperature sensors. In the case of the magnetometer, knowledge of the amplitude of the fluctuating magnetic field at the InSight lander will allow the separation of seismic signals from potentially interfering magnetic signals of either natural or spacecraft origin. To acquire such data, a triaxial fluxgate magnetometer was installed on the deck of the lander to obtain magnetic records at the same cadence as the seismometer. Similarly, a highly sensitive pressure sensor is carried by InSight to enable the removal of local ground-surface tilts due to advecting pressure perturbations. Finally, the local winds (speed and direction) and air temperature are estimated using a hot-film wind sensor with heritage from REMS on the Curiosity rover. When winds are too high, seismic signals can

The InSight Mission to Mars II
Edited by William B. Banerdt and Christopher T. Russell

✉ D. Banfield
banfield@astro.cornell.edu

¹ Cornell Center for Astrophysics and Planetary Science, Cornell University, Ithaca, NY, USA

² Centro de Astrobiología, Madrid, Spain

³ Earth, Planetary, and Space Sciences, University of California, Los Angeles, CA, USA

⁴ Department of Earth, Ocean and Atmospheric Sciences, University of British Columbia, Vancouver, BC, Canada

⁵ Planetary Science Institute, Tucson, AZ, USA

⁶ Jet Propulsion Laboratory, Pasadena, CA, USA

⁷ Tavis Corporation, Mariposa, CA, USA

⁸ Institut de Physique du Globe de Paris-Sorbonne Paris Cité, Université Paris Diderot, 75013, Paris, France

be ignored or discounted. Herein we describe the APSS sensor suite, the test programs for its components, and the possible additional science investigations it enables.

Keywords Spacecraft · Instruments · Magnetometer · Pressure · Wind · Temperature

1 Introduction

The NASA Discovery mission InSight (Interior Exploration using Seismic Investigations, Geodesy and Heat Transport) launched on May 5, 2018, will place a geophysical lander on Mars on November 26, 2018, to study its deep interior. The Surface Phase consists of the relatively short Deployment and Penetration Phases, followed by Science Monitoring. The nominal mission ends after one Mars year, plus 40 sols.

The science payload comprises three instruments: the Seismic Experiment for Interior Structure (SEIS), the Heat-Flow and Physical Properties Probe (HP³), and the Rotation and Interior Structure Experiment (RISE). RISE will use the spacecraft's X-band communication system to provide precise measurements of planetary rotation. SEIS and HP³ are placed on the surface with an Instrument Deployment System (IDS) comprising an Instrument Deployment Arm (IDA), Instrument Deployment Camera (IDC), and Instrument Context Camera (ICC). There are also several supporting instruments. The spacecraft instrumentation includes a radiometer (RAD) that will be used by the HP³ team to measure surface temperature and thermal properties to support their data analysis. The Auxiliary Payload Sensor Subsystem (APSS) collects environmental data in support of SEIS. This manuscript focuses on these sensors.

The APSS sensor suite consists of a magnetometer (InSight FluxGate or IFG), a pressure sensor (PS), and the Temperature and Wind for InSight (TWINS) pair of sensors. These sensors communicate with the spacecraft through the Payload Auxiliary Electronics (PAE), which collects their data, processes it, and sends it to the spacecraft computer several times a day. The APSS suite can operate even when the spacecraft itself is asleep, as the PAE and the various sensors can be powered independently of the main spacecraft computer, enabling data to be obtained continuously throughout a Martian sol. The PAE also includes a monitor of the spacecraft bus voltage that can also be recorded while the spacecraft sleeps.

The APSS sensors are included on this scientifically-focused mission to assist the SEIS instrument in obtaining clean and useful seismic signals. Environmental or lander-induced magnetic fields can produce signals on the sensitive seismometers not related to ground movements. By directly detecting the changing local magnetic field using the IFG sensor, the seismograms from SEIS may be corrected for these magnetic influences. Similarly, when strong winds are blowing, they could introduce noise to the seismograms. InSight measures the winds using TWINS to identify these periods when the winds are too strong to make good seismic measurements. TWINS also records the ambient atmospheric temperature, which can influence the SEIS instrument. Finally, the Pressure Sensor (PS) measures atmospheric pressure perturbations. These changes in the atmospheric loading on the surface result in small horizontal tilts of the ground surface, which are recorded by the sensitive seismometers. The pressure measurements allow removal (to the extent possible) of these tilt effects from the seismic signals (Kenda et al. 2017; Murdoch et al. 2017). In addition to their primary role in helping to produce a clean, interpretable data set from the SEIS instrument, the APSS sensors can also be used to study the environmental conditions at the InSight landing site for their own sake.

2 Measurement Objectives

2.1 SEIS Environmental Decorrelation and Event Diagnostics

InSight's SEIS instrument will be sensitive to both atmospheric pressure and magnetic fields at Mars. The pressure sensitivity will be primarily due to the deformation of the subsurface where SEIS will be installed. This effect is described in detail in Mimoun et al. (2017) and in Murdoch et al. (2017). Atmospheric pressure perturbations (high or low anomalies) can be thought of as point loads (with positive or negative sign) in the vicinity of the InSight lander, with the surface exhibiting an elastic deformation in response to the loading that is sensed by the SEIS instrument as time dependent tilts. The APSS pressure sensor will therefore be used to decorrelate the seismic data from this deformation signal, in a way similar to what is made on Earth (Zürn and Widmer 1995; Beauduin et al. 1996; Zürn et al. 2007). Realistic modeling of the surface deformation generated by large eddies have validated an improvement (reduction in the noise in the seismic signals) by more than a factor 5 at long periods (Murdoch et al. 2017; Lognonné et al. 2018).

Magnetic decorrelation is expected to be related to the direct effects of local magnetic fields on the various magnetic parts of the SEIS pendulum (i.e., the springs, the magnets of the micro-motors, the feedback mechanism, see details in Lognonné et al. 2018). Sensitivities are typically smaller than $0.5 \text{ nm/s}^{-2}/\text{nT}$ and have been validated on Earth (Forbriger et al. 2010).

2.2 Insight Fluxgate Magnetometer

The early exploration of Mars included magnetic sensors on every spacecraft. However, the early missions made observations at altitudes that were not suited for distinguishing a weak intrinsic magnetic field from one induced by the interaction with the solar wind. The first magnetic measurement at Mars was on Mariner 4 that flew by on July 15, 1965, at a distance of 3.9 Mars radii (R_M) (Smith 1969). These data revealed a standing bow shock, but the trajectory did not approach Mars sufficiently close to reveal whether this shock was associated with a weak intrinsic field or an ionosphere (Russell 1979). Subsequently, Mars 2 and Mars 3 entered large eccentric orbits about the planet on November 27, 1971, and December 2, 1971, in orbits of 1.3 by $9R_M$ and 1.3 by $63R_M$ (Dolginov et al. 1976). These measurements could also be interpreted as the draping of magnetic fields over the planetary ionosphere (Russell 1978), but Dolginov (1978a, 1978b) maintained his original interpretation of the data as an intrinsic field. A decade later, Phobos 2, the next successful Mars orbiter, carried a magnetometer but was also unable, from the high-altitude orbit designed to study Phobos, to distinguish unambiguously an intrinsic Martian magnetic field contribution to the magnetic field associated with the solar wind interaction (Yeroshenko et al. 1990). The OPTIMISM magnetometer (Kuhnke et al. 1998), companion instrument of the OPTIMISM seismometer (Lognonné et al. 1998) which had been expected to land on Mars in the Mars 96 small stations, was not successful either due to its failure during launch in November 1996. Finally, in 1997, the Mars Global Surveyor (MGS) made measurements at sufficiently low altitudes (reaching below the bottom of the ionosphere) to reveal magnetized regions in the Martian crust resulting from magnetization by an ancient dynamo field (Acuna et al. 1999).

MGS continued to provide almost full planetary coverage at around 400 km altitude while the Mars Atmosphere and Volatile Evolution (MAVEN) mission has been adding magnetic field measurements at altitudes above 125 km (Connerney et al. 2015). This results

Table 1 APSS sensor performance requirements

IFG	Noise < 0.1 nT/sqrt(Hz) from 0.01–1 Hz
PS	Noise < 10^{-2} Pa/sqrt(Hz) from 1–0.1 Hz
	Noise < $10^{-2} (f/0.1 \text{ Hz})^{-2/3}$ Pa/sqrt(Hz) from 0.1–0.01 Hz
TWINS	Detect when wind > 5.5 ± 1.5 m/s

in detailed coverage and models of the crustal magnetic field using only MGS (e.g., Langlais et al. 2004; Morschhauser et al. 2014) and both data sets combined (Mittelholz et al. 2018).

The Martian crustal magnetic field is highly nonuniform spatially and strong magnetic anomalies are mostly concentrated in the Southern hemisphere (Acuna et al. 1999). The crustal field signature around the InSight landing site shows weak but non-zero magnetization, from ~ 200 km altitude orbit and resulting crustal field models (see Fig. 5 in Mittelholz et al. (2017) and Fig. 6 in Smrekar et al. (2018) for magnetic field models around the landing site). Note that signals with length-scales much less than the spacecraft altitude are not resolvable from orbit and thus the small-scale magnetization at the surface might be greater than predicted.

InSight will provide us with magnetic field measurements on the ground. These will include periodic (Mittelholz et al. 2017; Langlais et al. 2017) and aperiodic magnetic variations of the field from currents in the ionosphere impressed by the solar wind interaction with the ionosphere. Data measured by the IFG will provide unique magnetic field information that can provide insight into ionospheric fields, and the electromagnetic properties of Mars' interior. Aspects of interior geophysics of the crust and mantle that may be able to be probed by IFG measurements are discussed in a companion paper by Smrekar et al. (2018).

Mars has a weak planetary magnetic field that is concentrated in magnetic “anomalies,” crustal regions that became magnetized eons ago when Mars possessed an internal geomagnetic dynamo (Acuna et al. 1999). InSight is targeted far from the nearest magnetic anomaly, and we expect to detect, at most, a weak remnant magnetic field together with a diurnal magnetic variation of the magnetic field from currents in the ionosphere impressed by the solar wind interaction with the ionosphere.

While MGS and MAVEN have made dips into the atmosphere, these dips have not allowed determination of the short-wavelength intrinsic magnetic field over the entire surface or the time variations of the magnetic field expected to be seen on the surface. Furthermore, the MAVEN data convolve the temporal and spatial variations of the crustal field. To determine the ionospheric field in the atmosphere, we turn to Venus, a planet that has been reported to have a negligible intrinsic magnetic field (Russell et al. 1980). Recently, the region beneath the ionosphere has been probed by Venus Express in a series of dips down to 130 km altitude (Zhang et al. 2016). Figure 1 shows these magnetic records as a function of altitude. Below about 140 km, the field appears to become quieter as if there were no longer currents flowing near the spacecraft. The field here is determined by the high-altitude currents in the ionosphere and any induced currents in the core. The decrease in field strength from 150 km altitude to 130 km indicates that the field strength measured by MAVEN in the magnetosheath and ionosphere is not necessarily that being impressed on the core.

We can model the fields expected at the InSight FluxGate (IFG) using a magnetostatic approach with an imposed high-altitude ionospheric field and a superconducting core inside the planet. The geometry of the current system and a putative core are illustrated in Fig. 2. Both Venus and Mars rotate and any magnetometer on the surface will sense a diurnal pattern as the magnetometer passes under the dayside ionosphere and later the nighttime or tail region. The size and conductivity of the electrically conducting core (as well as the electrical

Fig. 1 Sixty-six low-altitude profiles of the Venus magnetic field strength, the amplitude of the variance and the normalized varying field. The light traces show median values (Zhang et al. 2016)

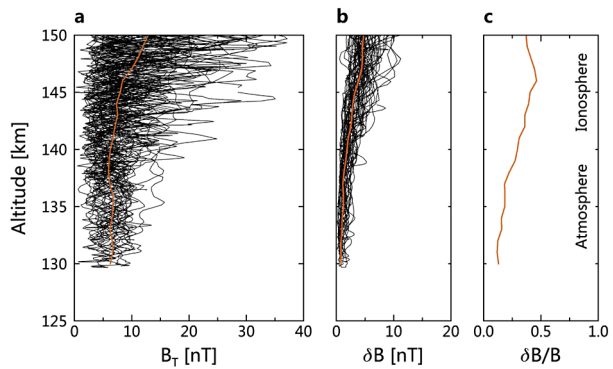
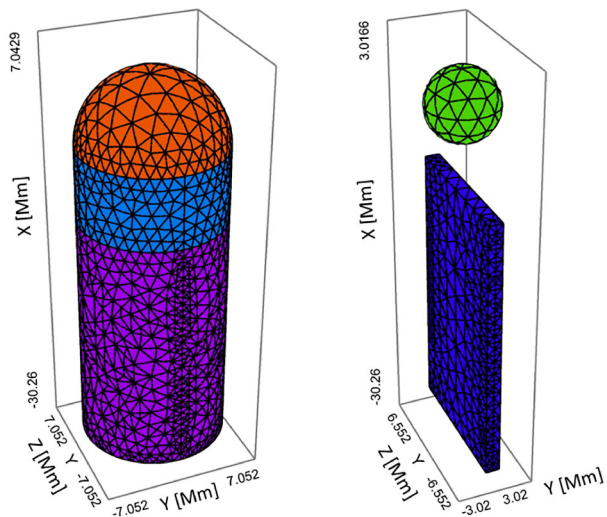


Fig. 2 Finite element meshes for the magnetopause current (left), the tail current sheet, and a core (right) used to model induced field seen in Venus' atmosphere. X points to the Sun

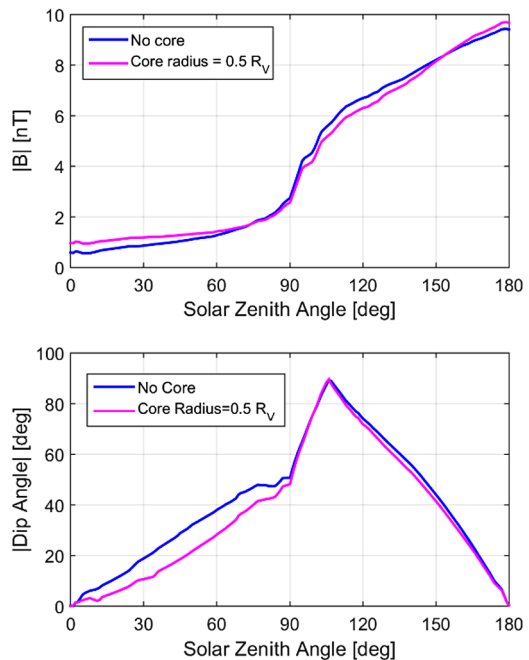


conductivity structure of the mantle, neglected here, but discussed in Smrekar et al. 2018) determines the amplitude of the induced diurnal signal. Using this simple magnetostatic geometry, we obtain the diurnal variation shown in Fig. 3.

While the diurnal variation of the field can provide an estimate of the size of the core, we may also be able to deduce bounds on the electrical conductivity profile of the crust and mantle by examining both the diurnal variation and the shorter time scale variations of the external conditions and the magnetic response to these higher frequency changes (Smrekar et al. 2018). The combination of MAVEN and InSight measurements may provide the means to separate the induced response and time varying external signals as discussed in the accompanying manuscript by Smrekar et al. (2018).

To calculate the magnetic field in the ionosphere requires measurements in the solar wind or in the ionosphere with a spacecraft instrumented with plasma and field instruments such as those of MAVEN. At higher frequencies, the magnetometer might detect atmospheric phenomena at Mars, such as the transient electric currents associated with lightning and possibly electric currents associated with dust devils, although no such signals have been yet detected (Gurnett et al. 2010).

Fig. 3 Expected field variation with solar zenith angle in field magnitude on the surface and the dip angle with and without a core for the ionospheric boundary shown above



2.3 Pressure Sensor & TWINS

In addition to their roles in improving the fidelity of the SEIS data against environmental perturbations, the pressure sensor (PS) and temperature and wind sensors (TWINS) on InSight can be used to advance fundamental atmospheric science goals at Mars. These atmospheric scientific capabilities of the InSight lander are detailed in much more depth in Spiga et al. (2018); however we will briefly discuss them here.

InSight will be the first Mars lander to effectively capture truly continuous pressure, air temperature and wind measurements. While the Viking Landers, Pathfinder, Phoenix and MSL have recorded environmental data at moderate sampling rate and (in the case of the Vikings and MSL) for long durations, there were inevitable data gaps in those data sets. InSight will return truly continuous data at a moderate sampling rate, but those periods that appear interesting in the moderate sampling rate data can be downlinked to Earth at the full sampling rate of InSight's sensors. InSight will be able to assess the threshold wind speed for Aeolian processes to move grains on the surface. With the data gaps in prior missions' environmental records, a specific peak wind speed associated with an observed change in the grains around a lander could not be made because that peak may have occurred during a data gap. Because of this, the actual wind speed required to move grains has not yet been established for Mars.

The pressure sensor is significantly more sensitive than its predecessors, with a typical observational noise of about 10 mPa. Additionally, it is equipped with a special Quad-disk probe inlet, designed to minimize the effects of winds, which could contaminate a true pressure measurement by creating dynamical pressures on the pressure sensor. Finally, its sampling rate is 20 Hz (although the response time of the inlet system is about one third this). All of these combine to enable the pressure sensor to detect known phenomena on Mars (e.g., dust devils) with more precision and farther from the lander, as well as new phenomena that are as-yet only speculated (e.g., infrasound as in Williams 2001, and Garcia et al.

2017). Recently, at the nearby equatorial site, the signal of mid-latitude baroclinic waves was identified in MSL data (Haberle et al. 2018). InSight's significantly lower noise floor should help clarify and extend that record to a second location, and a longer duration. Having a second pressure sensor within a few hundred km of MSL will also prove interesting as a network of two relatively nearby stations can be used to discern the larger-scale structure of pressure systems that pass by both landers. The pressure sensor on InSight is expected to have only a modest temporal drift in its absolute calibration (as measured between two sets of ground calibrations, the first in 2015, and the other in 2017). The question of whether the atmospheric pressure is secularly changing has been discussed in Haberle and Kahre (2010), and may be clarified by InSight's pressure measurements.

3 Design Requirements

3.1 Insight Fluxgate Magnetometer

The design requirements for IFG included measuring the magnetic fields that would be experienced on the lander. The range of the sensor needed to exceed the sum of any planetary magnetic field and any spacecraft magnetic field. Additionally, because of the magnetic sensitivity of the SEIS instrument (specifically the VBB), the expected magnetic field time variation will be a source of noise on the seismometer. As magnetic shielding with mu-metal was not compatible with the maximum mass supported by the deployment arm, the IFG is included to quantify and decorrelate the magnetic-field induced noise from the seismic signals. The landing site is at longitude 136°E and latitude 4.5°N (Golombek et al. 2018), in a region of weak magnetic field (Mittelholz et al. 2018). Because of this, we expect the planetary magnetic field to be well-estimated by those shown in Fig. 3, on the order of 10 nT. After instituting a test program to verify the expected magnetic fields induced by the lander activities (e.g., 100–1000 nT), we chose a range for the magnetometer of $\pm 20,000$ nT. The sensitivity requirement of IFG was determined by considering the magnetic field strength that could impact the SEIS sensor. The SEIS (VBB) magnetic sensitivity has been measured as $< 0.5 \text{ nm/s}^2/\text{nT}$. If we require the residual noise from the magnetic fields to be well below the SEIS acceleration requirement ($1 \text{ nm/s}^2/\sqrt{\text{Hz}}$), this leads to an IFG noise requirement of $< 0.1 \text{ nT}/\sqrt{\text{Hz}}$ at 0.01 Hz (see Table 1). The SEIS bandpass goes from 0.01–20 Hz, so this was also the bandpass requirement for IFG. Within this frequency range, the digitization allows signals with amplitudes of 5 pT to be measured. The diurnal variation of the magnetic field on the surface is expected to be about 2500 times this value, i.e. about 12 nT from Fig. 1. The typical noise levels on the IFG are shown in Fig. 8 to be well below this requirement throughout the bandpass.

3.2 Pressure Sensor

The main reason for inclusion of the PS on InSight is to help identify atmospheric pressure variations that may induce tilts on the ground surface around the lander, and where possible, enable the removal of these atmospheric-pressure induced tilts (e.g., Murdoch et al. 2017). In addition to larger scale pressure systems, smaller atmospheric phenomena like dust devils (or more generally, vortices) can also induce local tilts around the lander, and should also be detectable by PS (e.g., Kenda et al. 2017, cf. Lorenz et al. 2015). The need to realize these capabilities establishes the requirements for InSight's pressure sensor. The first requirement is that the bandpass of the pressure sensor again match the SEIS instrument

(much like with IFG). Thus, the pressure sensor was required to be sampled at 20 Hz, with a full response below 1 Hz. In the main SEIS bandpass, from 0.01–1 Hz, the PS would need to achieve a very low noise spectrum to yield sufficiently high-quality observations to enable the removal of these atmospheric effects from the SEIS signals (Lognonné et al. 2018). These noise floor requirements can be expressed as 10^{-2} Pa/sqrt(Hz) from 0.1–1 Hz, and $10^{-2} (f/0.1 \text{ Hz})^{-2/3}$ Pa/sqrt(Hz) from 0.1 to 0.01 Hz (see Table 1). When used to decorrelate the SEIS data, the pressure data will inject in the final acceleration signal the self-noise of the pressure sensor. The latter can be expressed as $ng = Cnp$, where C is the compliance of the ground in $\text{m/s}^2/\text{Pa}$, np is the pressure self-noise in Pa/sqrt(Hz) and ng is the equivalent ground acceleration noise in $\text{m/s}^2/\text{sqrt(Hz)}$. As shown by Fig. 2 of Kenda et al. (2017), the compliance of the Martian regolith is expected to generate vertical displacement of about 1 nm/Pa at 0.5 Hz, which is expected to be the frequency where the body waves will have their best detection threshold for the continuous 2sps VBB data. This is corresponding to a vertical acceleration sensitivity of about $10 \text{ nm/s}^2/\text{Pa}$ with respect to a pressure change. The requirement of the pressure sensor was set in order to have a pressure self-noise equivalent to 1/10 the SEIS full requirement which is $1 \text{ nm/s}^2/\text{sqrt(Hz)}$. This leads to a pressure requirement of 0.01 Pa/sqrt(Hz) in the body wave bandwidth (0.1–1 Hz) which is the most critical and challenging from instrument design perspectives. The pressure sensor was demonstrated to have met these noise spectrum requirements in ground testing (see Fig. 18).

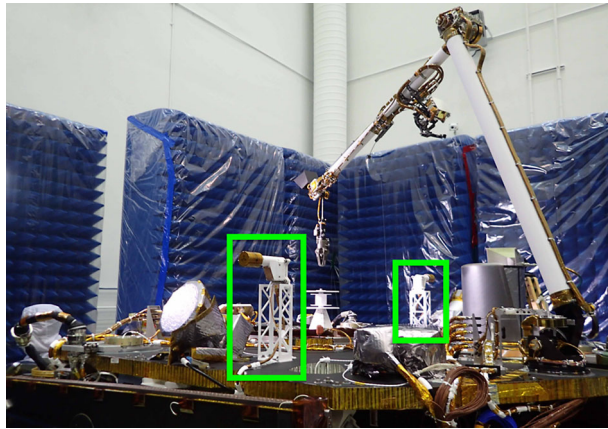
The atmospheric pressure and its significant annual variations must also remain within the pressure sensor's calibrated range throughout a full Mars year. Based on the landing site, atmospheric modeling indicates this range should span from 560–950 Pa annually (private communication, Michael Mischna and David Kass, 2015).

3.3 TWINS

The TWINS instrument will help determine the best possible conditions to deploy the SEIS and HP3 instruments after the first commissioning sols on Mars, but primarily will contribute to reducing the false-positive seismic events that may be caused by environmental phenomena rather than Marsquakes or meteorite impacts. Toward this goal, it is required that TWINS be capable of determining, by ground analysis of measurements, when the wind at the mounting height of the sensor exceeds $5.5 \text{ m/s} \pm 1.5 \text{ m/s}$ (see Table 1). Correspondingly, in support of these wind measurements, the TWINS ambient temperature sensor will be able to measure the environmental temperature in the range 167 K to 277 K, with an accuracy of 6 K, and a sampling rate of 1 Hz. These performance requirements were established by estimating the wind speeds above which wind would produce seismic noise above the SEIS performance threshold of 10^{-9} m/s^2 (Lognonné and Mosser 1993). For winds above this, the SEIS instrument's measurements will be saturated with wind noise and we will disregard those times.

However, TWINS' wind and ambient temperature sensors will also provide valuable atmospheric data that, especially in combination with PS, will help better understand the atmosphere boundary layer at the landing site based on the thermal state, air motions and pressure. These secondary but valuable objectives in turn dictate a specific set of measurements, with extended requirements. The diurnal variation of air temperature will not be less than 10 K in dusty conditions, and not more than 100 K under clear skies. The accuracy levels of the air temperatures must, at least, allow diurnal cycle monitoring under even the dustiest of conditions. For this extended scenario, it is required that TWINS is capable of measuring the temperature of the air near the booms, over the range of 150 to 300 K, with a resolution of 0.1 K, and an accuracy of 5 K.

Fig. 4 TWINS booms over the InSight platform, during the final integration and test phase. The picture also shows all the elements that will remain on the deck after deployment. All these elements, with the exception of the IDA (Arm) and the HGA antenna (gray cylinder on the right), are shorter than the TWINS booms, not causing a significant perturbation on the winds measurements once the surface elements are deployed. The Pressure Sensor Quad-Disk inlet is seen in the center of the deck, between the two TWINS booms



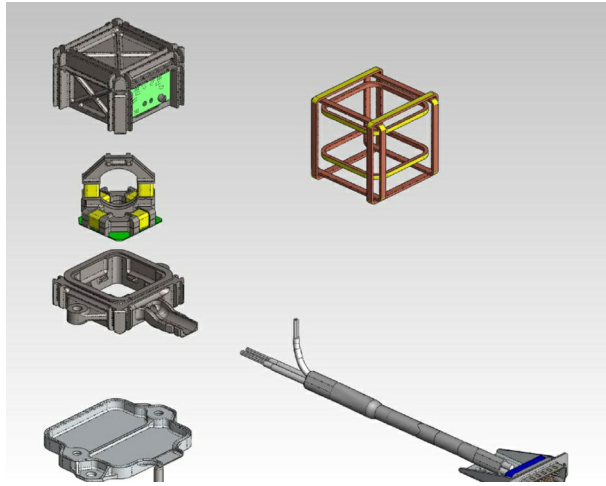
The wind sensor, aiming to characterize the wind variations caused by the local components of the circulation, will be able to provide the wind speed and direction at the sensor level, for both booms, with a relative accuracy of $\pm 15\%$ in the range of 1–60 m/s, and at 1 Hz. The resolution provided by the wind sensors is better than 0.4 m/s in low wind speeds, and 2 m/s in high speeds. Additionally, TWINS' wind sensor will be able to measure the direction of the horizontal winds with a resolution and accuracy better than 22 degrees. Thus, TWINS exceeds the performance requirements for the mission.

TWINS will also be able to measure vertical winds in the range of 0 to 20 m/s. However, given the low height of the booms with respect to the deck, the number of surrounding wind-perturbing elements on top of the platform (Fig. 4), and the low nominal downlink data rate, the precision of TWINS' wind and temperature estimates may be impaired. To mitigate this uncertainty due to flow obstructions, the ground processing of the data recorded by TWINS will also take into account a number of Computational Fluid Dynamics (CFD) simulations that consider the wind-perturbing elements and, together with the calibration data, finally result in an estimate of the free-flow wind.

3.4 Payload Auxiliary Electronics

In addition to the three main sensors that comprise APSS, there is also a set of electronics to control these sensors, receive and distribute power and commands from the lander, log their data throughout the day, and then transmit these data to the spacecraft's main computer for eventual playback to Earth. This system is known as the Payload Auxiliary Electronics (PAE). The PAE therefore must be commandable by the spacecraft's main computer to set operating parameters (including powering them on or off) for each of IFG, PS and TWINS. The APSS, through the PAE, can be operated with any combination of these science sensors. Additionally, the PAE must be able to receive and temporarily store data from these sensors, and then eventually send them on (typically several times a day) to the spacecraft computer. In the case of the PS data, PAE also performs signal processing on the quickly sampled analog output from PS to deliver it as a 20 Hz sampled digital signal. Finally, because PAE operates continuously on InSight, and the spacecraft computer does not, the PAE includes an additional channel to monitor the spacecraft bus voltage continuously.

Fig. 5 (Left) Exploded diagram of fluxgate magnetometer. (Top to bottom) Housing, cores, base mounting plate. (Right top) Feedback coils. (Right bottom) Pigtail connector



4 Instrument Description

4.1 InSight Fluxgate Magnetometer

4.1.1 Sensor Description

The InSight fluxgate magnetometer (IFG) consists of a single triaxial fluxgate magnetometer with a range of $\pm 20,000$ nT and a sample rate of up to 20 Hz. This signal may be low-pass filtered before being transmitted to Earth at times of low available bandwidth. The sensors have extensive heritage from the Magnetospheric Multiscale (MMS) mission in Earth orbit, where eight such sensors were used (Russell et al. 2016). The sensor is mounted under the deck on the side facing the SEIS deployment. The electronics are housed with the Payload Auxiliary Electronics (PAE). Figure 5 shows some of the components of the fluxgate sensor. The diagram on the left shows the two fluxgate cores and their six sense-windings. Each pair of windings provides sensitivity to the magnetic field component in one of the three orthogonal directions. The magnetic field surrounding the sensors is nulled by a triaxial arrangement of feedback coils in the right-hand panel of Fig. 5. The three feedback currents are controlled by the sense windings around each coil pair. The sensor is connected to the PAE by a cable of 2.5 m in length. The amount of current needed to null the ambient field gives the field strength.

The sensor is a simple assembly, as illustrated in the exploded diagram of Fig. 5. The two ring cores fit inside the two housing parts, about which the feedback coils are wound. Figure 6 shows the assembled sensor with its white dust cover, as appropriate in the dusty Mars environment. The sensor with its cover and pigtail has a mass of 171 g and dimensions $75 \times 74 \times 52$ mm³. The sensors were thermally cycled 2127 times over the temperature range -105°C and $+25^{\circ}\text{C}$ to qualify them for flight.

A dynamic range of $\pm 20,000$ nT was chosen so that the unit will not saturate in the magnetic field of the lander and the environment. The sensor is mounted on the deck of the Lander, and its electronics unit is in the PAE box and connected to it by a cable. The electronics unit (Fig. 7) is $14 \times 10 \times 1.4$ cm and digitizes analog signals from the magnetometer sensors using the 16.384 MHz clock provided by the processor board. The electronics board has a mass of 101 g and resides across the deck in the APSS chassis. The cable mass is

Fig. 6 InSight magnetic sensor with dust cover and pigtail

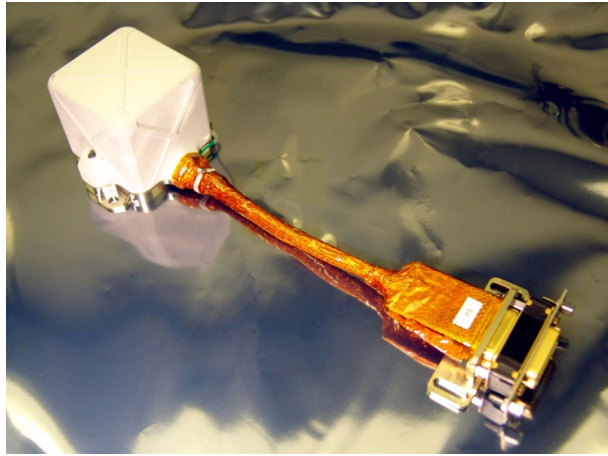


Fig. 7 Electronics board of IFG, which is housed in the PAE electronics chassis



286 g. The total power required is 1 W. The electronics board uses +8 V power provided by the PAE and converts this voltage to those required by the electronics. The magnetometer transmits three 24-bit magnetic field components (X, Y, Z) together with housekeeping information at a rate of 20 vectors per second to the processing and telemetry system, which can average the data and perform statistical analysis on the data prior to transmission. The noise level of the magnetometers is shown in Fig. 8. The pointing knowledge required by this investigation is $\pm 1^\circ$ relative to the spacecraft axis, and there is no absolute pointing requirement relative to geographic coordinates levied by the science goals; the pointing knowledge of the spacecraft is sufficient.

4.1.2 Testing

The IFG was calibrated in the UCLA magnetics facility over the expected operating temperature range. The tests provided data on alignment and linearity. Once installed on the spacecraft deck, the region around the sensor was probed for local field gradients with test magnetometers. While local gradients were found, none were seen that suggested the presence of strong magnetic fields near the sensor. Toward the end of spacecraft testing in 2015,

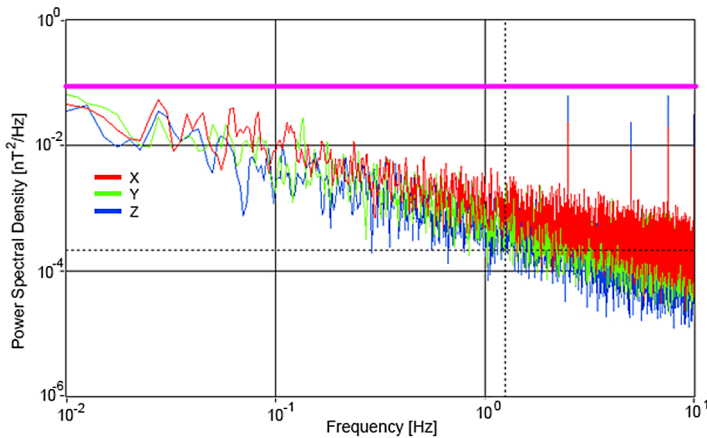


Fig. 8 Noise in each axis as a function of frequency for the IFG instrument. *X*-axis noise is in red, *y*-axis in green, and *z*-axis in blue. The requirement is in pink

the magnetic moment of the spacecraft was determined by a swing test with the spacecraft suspended above the floor. The location of the spacecraft during the swings and the orientation were determined by laser trackers. The three components of the magnetic field in the Lockheed facility from one of the facility magnetometers during the test are shown in Fig. 9. These data were inverted to obtain the magnetic field due to the magnetic moment of the lander. The magnetic field due to the spacecraft moment at the location of the sensor was then calculated to be (564, −515, 71) nT in the spacecraft coordinate system with an rms error of 16 nT. This was well within the $\pm 20,000$ nT range of the instrument. With the spacecraft firmly on the test platform, magnetic changes associated with commanding were monitored with several test magnetometers arranged around the spacecraft to measure the gradients between the sensor location, as well as the expected SEIS sensor placement. Step function changes were observed with some commands, such as UHF power and SDST on. These will be removable if they recur on the Martian surface. Other commands produced transients such as UHF transmit and the EPS relay. An illumination test was performed and no discernible fields were generated in a 0.7 Amp test. When the solar panels were deployed, only a small magnetic disturbance was detected.

In October 2017, a second test was performed to verify the spacecraft magnetic field had remained low. This test was static in which the spacecraft remained in a single location and only the magnetometers moved. As shown in Fig. 10, the outer edge of the spacecraft was surrounded with 6 equi-spaced magnetometers at the level of the platform and some distance back from the edge of the spacecraft. Then two magnetometer stands were placed close to the edge of the spacecraft on either side, aligned with two of the ‘external’ magnetometers along a line through the center of the spacecraft. Each stand had a magnetometer below the deck level and one above the deck level. Measurements were then obtained at three distances between the spacecraft and the outer circle on both sides of the spacecraft. This was repeated for the two other magnetometer lines across the spacecraft.

The magnetic measurements were then used to determine the spatial gradients centered on the spacecraft, and to identify field sources that could not possibly be on the spacecraft. Three large sources were found that could only be due to equipment in the facility, and these fields were modeled and removed from consideration; finally one source remained that could be part of the spacecraft. This source was then used to calculate the field at the fluxgate

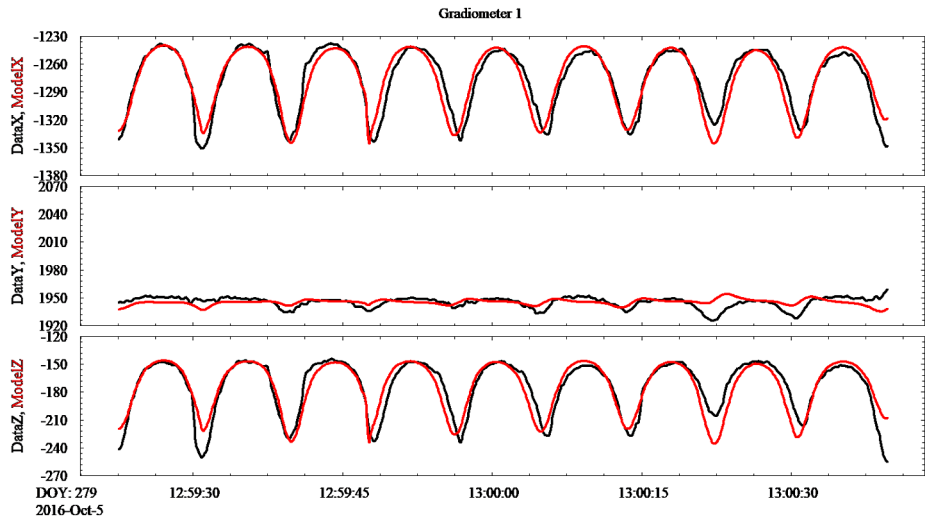


Fig. 9 Swing test. Magnetic field at one of the laboratory magnetometers surrounding the swinging suspended spacecraft. Black curve is observed field; red curve is modeled

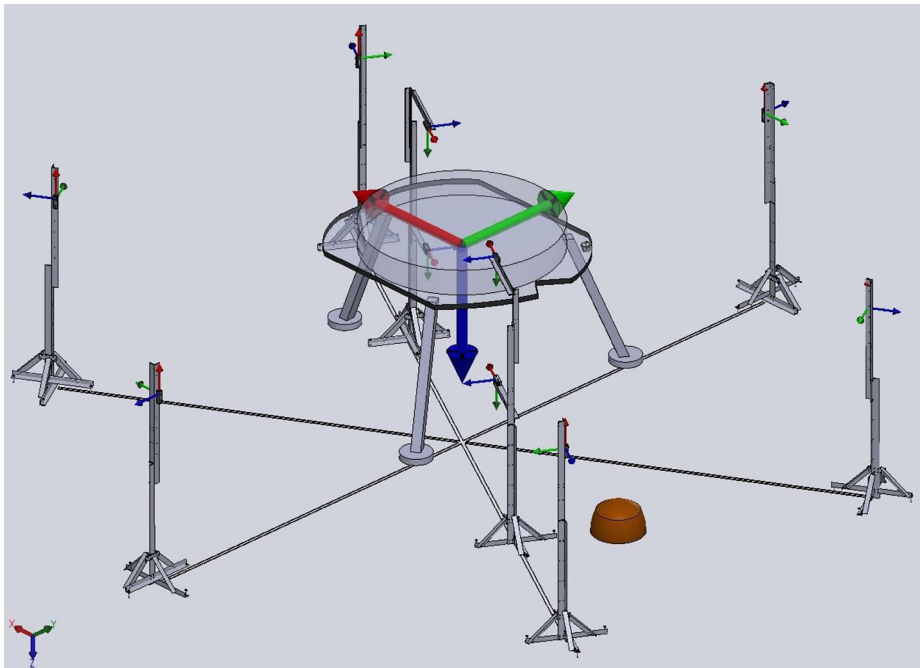
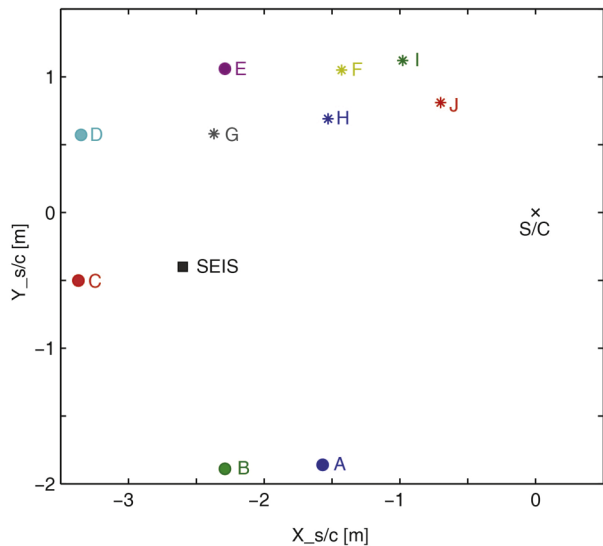


Fig. 10 Magnetometer configuration for static field gradiometer measurement

sensor. This field was $(534, -353, -18)$ nT. This is very similar to the value deduced from the swing test data. The interplanetary operation of the magnetometer will be the final arbiter of the zero levels of the magnetic measurement.

Fig. 11 Location of test magnetometer relative to center of spacecraft and SEIS deployment region during commanding test



4.1.3 Transient Field Testing

During subsequent testing of the spacecraft, it was noted that a subset of the commands caused at least transient magnetic signals to occur around the spacecraft. A list of these commands and their effects were compiled.

Again, ten magnetometers were placed around the spacecraft at distances ranging from 1.1 m to 3.7 m, monitoring the magnetic field from October 16–20, 2017, during which time the spacecraft commands were tested. The locations, shown in Fig. 11, were chosen to best define magnetic fields near the SEIS deployment region. When more than five magnetometers detect an impulse and the largest perturbation is over 10 nT, the impulse is identified as a signal. In total, 1938 such signals have been recorded.

The 79640 commands are classified into 3091 groups, as many of the same or similar commands were sent multiple times. The most frequent commands are related to data transfer and status checking, which are not expected to generate significant magnetic perturbations. We focus on the commands, requesting the spacecraft or its devices to change modes. If those commands were sent within 60 s before a magnetic perturbation, the commands were suspected to be the causes of the magnetic perturbations. Examples of the transient signals recorded in the vertical direction for the locations shown in Fig. 11 are presented in Fig. 12. After landing we will determine which of these 3091 command groups are producing magnetic signals on Mars that may be detected by SEIS. We will then use our test data to extrapolate from IFG to the SEIS location, so that IFG recordings can be used to decorrelate any spacecraft magnetic signals from the SEIS signals.

4.2 Pressure Sensor

The PS consists of a pressure transducer, manufactured by the TAVIS corporation (Fig. 13, left), a special inlet fitting, and a set of tubing to connect the inlet to the sensor. The inlet probe is specifically designed to minimize the effects of wind on the pressure measurement, with a design similar to the “Quad-Disk” design developed for single inlet microbarometric measurements terrestrially (Nishiyama and Bedard 1991, hereafter N&B) (Fig. 13, right).

Fig. 12 Example of the vertical component signals recorded by the test magnetometers during the transient field test

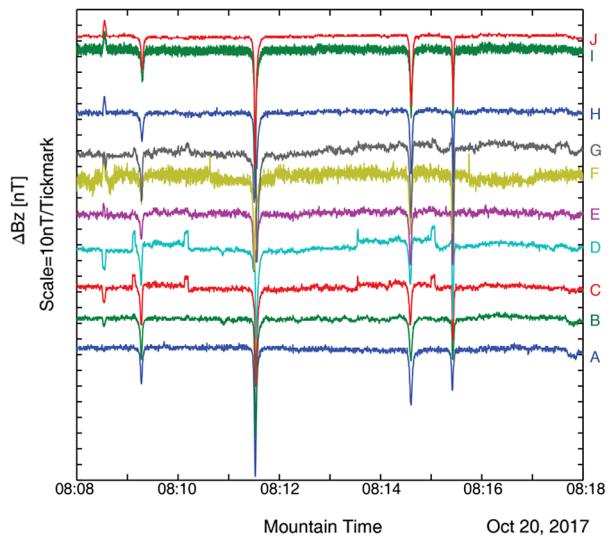
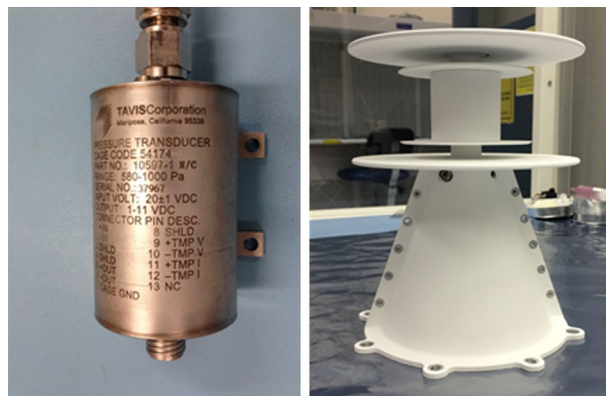


Fig. 13 (Left) The InSight Pressure Sensor. (Right) the Quad-Disk Probe inlet modified from terrestrial versions to perform better under Mars atmospheric conditions



The inlet is placed near the center of the lander deck, and is covered by the WTS (Wind & Thermal Shield) in its stowed configuration until deployment. After deployment, the inlet is exposed directly to the ambient winds, albeit with the wind perturbations from the lander itself and the deck obstacles. The sensor is within the body of the lander, giving it a relatively benign and stable thermal environment from which to make its measurements. The separation between the inlet and the sensor drives the need for the tubing to connect the two components.

4.2.1 Quad-Disk Probe and Inlet Tubing

Quad-Disk (QD) probes have been used extensively to obtain steady-state and transient measurements of the static pressure in terrestrial environments (e.g., see Massman et al. 1997; Nishida et al. 2005) since their inception almost three decades ago. The principle of operation, its main elements and results from wind tunnel tests of the original design are presented by its developers in Nishiyama and Bedard (N&B). A schematic of the probe showing its main elements based on the N&B design is illustrated in Fig. 14. Referring to

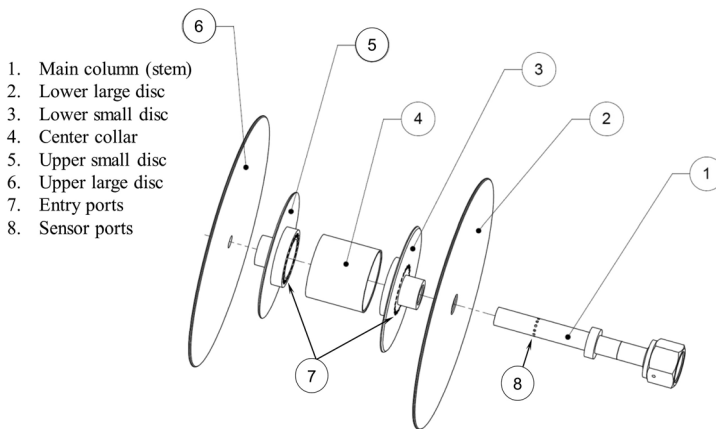


Fig. 14 Schematic showing the basic elements of the Quad Disk static pressure probe based on the design of Nishiyama and Bedard (1991)

the schematic, the basic principle of operation is that as flow passes through the spacing between each pair of disks, and over the entry ports at both ends of the center collar, the combined average of the pressure at an upper and a lower set of entry ports becomes close to the true static pressure when the angle of attack α is near zero. When $\alpha > 0$, different average pressures will be attained at the upper and lower entry ports, but these typically sum to zero at the sensor ports located at the mid-length of the collar, if α is not too large. The QD was chosen for InSight mainly due to the accuracy with which it can provide the true static pressure within a desirable range of frequencies. In this section, we report on our estimates of the expected frequency-dependent damping of the pressure signal on Mars by the QD, and on analyses and flow visualization tests aimed at assessing errors in the measurements that are associated with induced turbulence.

To determine the dynamic response of InSight's QD system, we refer to the idealized schematic in Fig. 15, depicting the most basic elements of a single line-cavity pressure sensor. It consists of a tube with a high aspect ratio ℓ/d that connects the inlet pressure port to the chamber volume. The latter contains the pressure transducer. Here ℓ and d are the length and diameter of the tube, respectively. If the pressure signal at the inlet is $p_i(t)$ then as the flow traverses the tube it will transmit a different signal $p_o(t)$ to the transducer (Fig. 15, left), because the original signal is damped by viscous effects. The transducer then generates an electrical signal that is a function of $p_o(t)$. Our objective here is to determine the so-called amplitude modulation (A), which is a measure of how much the amplitude of the signal is weakened as the fluid traverses the sensor tubing.

First, we express the pressure signal as a sinusoid over a mean value \bar{p} as follows:

$$p(t) = \bar{p} + \delta p \cos(\omega t) \quad (1)$$

where δp is the pressure amplitude relative to \bar{p} . It can easily be shown that the response of such a system is analogous to that of a series-RLC electrical circuit which is known to have a natural frequency $\omega_n^2 = 1/LC$ and damping factor $\xi = R/2L\omega_n$. Here R , L and C are the resistance, inductance and capacitance of the electrical circuit, respectively. The damping factor ξ is a measure of the amount by which the oscillations of the circuit decrease over time. The analogy with the RLC circuit stems from the fact that the governing equation

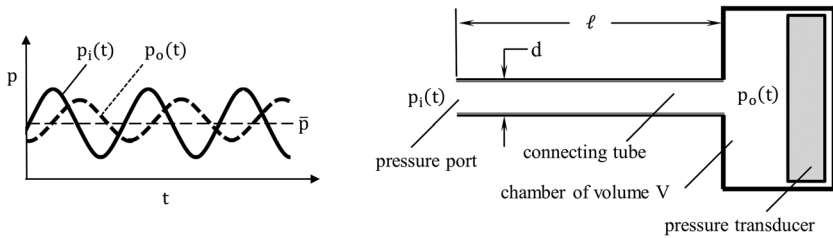


Fig. 15 The modulation of the ambient pressure signal (left) as it is transmitted through a line-cavity pressure sensor consisting of a long tube that connects the pressure port to the chamber containing the transducer (right)

for the flow in a line-cavity pressure sensor can be modeled as an incompressible laminar viscous flow in which the pressure drop across the connecting tube is determined by the Hagen–Poiseuille law. Then R is due to pressure viscous losses, L is due to the inertia of the fluid and C is the capacity of the transducer to allow for the storage of flow energy in the chamber volume. The following scalings are therefore expected for the three circuit element properties:

$$R \sim \frac{\mu \ell}{d^4} \quad L \sim \frac{\rho \ell}{d^2} \quad C \sim \frac{V}{\rho a^2} \quad (2)$$

where μ and ρ are the dynamic viscosity and mass density of the fluid, respectively. The speed of sound in the flow is denoted as a . Following these scalings, the amplitude modulation can be determined (Holman and Gajda 1978; Wilczak and Bedard 2004) from:

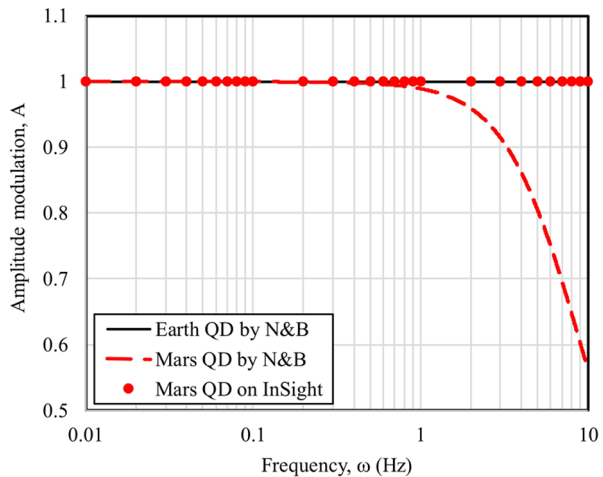
$$A^2 \equiv \left(\frac{\delta p_o}{\delta p_i} \right)^2 = [(1 - f^2)^2 + (\xi f)^2]^{-1} \quad (3)$$

where

$$f = \frac{\omega}{\omega_n} \quad \omega_n = \frac{da}{4} \sqrt{\frac{3\pi}{\ell V}} \quad \xi = \frac{32\mu}{\rho a d^3} \sqrt{\frac{3\ell V}{\pi}} \quad (4)$$

For illustrative purposes, we compare in Fig. 16 the estimated amplitude modulation spectrum of the N&B QD (dimensions provided in N&B) on Earth and Mars. For the terrestrial conditions, we have assumed $\mu = 1.812 \times 10^{-5}$ Pa/s, $\rho = 1.225$ kg/m³ and $a = 340$ m/s. For Mars we have taken the following typical conditions: $\mu = 1.223 \times 10^{-5}$ Pa/s, $\rho = 2.2 \times 10^{-2}$ kg/m³ and $a = 249$ m/s. Clearly, with the viscosity and speed of sound being comparable in the two atmospheres, the largest impact on the modulation of the signal is due to the difference between the mass densities. More specifically, on Earth the damping factor ξ is reduced significantly due to the $\sim 50\times$ higher density compared to that on Mars as can be seen by Eq. (4). Under Martian conditions we estimate the modulation of the signal to be reduced by about 1% of its original amplitude at 1 Hz for the N&B design, and to fall off sharply for higher frequencies, effectively making it a low-pass filter with a cut-off near 1 Hz. To increase the high frequency performance under Martian conditions, the geometry of the QD for InSight was modified somewhat from the N&B design. For the InSight design, the predicted modulation would only fall by 1% of its original value at a frequency of ~ 170 Hz (see Fig. 16). Thus, the InSight design should not be mechanically low-pass filtered by its Quad-Disk design for the sensor's sensitivity up to 20 Hz.

Fig. 16 Estimates of the pressure signal modulation on Earth and Mars for the QD designed by N&B. Also shown is the estimate on Mars for the design used on InSight



It is well-known that turbulence can affect adversely static-pressure measurements (e.g. see Bradshaw and Goodman 1968; Christiansen and Bradshaw 1981). Errors stated in the literature are typically $\sim 1\%$ relative to the dynamic pressure for turbulence intensities (TI) $< 10\%$. However, corrections of this kind are uncertain because errors depend not only on TI but also on the length scale of turbulence, its structure, and presence of coherent (organized) fluid motions. For the QD, the impact of the turbulence would become more adverse if its characteristic length scale became comparable to or smaller than the size of the device. The main source for such turbulence on InSight that could interfere with the accuracy of the ambient pressure measurement would be flow separation over the QD disks and/or over the elements on the rover deck that surround it.

In regards to the latter, our analyses showed that most of the elements on the deck will not produce interference that will affect the pressure measurements significantly. Of particular interest was the UHF antenna because its size is comparable to the QD, and therefore vortex shedding due to flow over it could produce turbulence of scale lengths comparable to the size of the QD. To better quantify the effect on the pressure measurement, we performed Large Eddy Simulations of flow over an idealized geometry of the antenna to compute the vortex shedding frequencies. We found that for mean wind speeds on Mars (~ 5.7 m/s, Hess et al. 1977; Ryan et al. 1978; Murphy et al. 1990), these shedding frequencies were larger than 2.5 Hz and therefore outside the required operational range of the sensor (0.01–1 Hz). At lower wind speeds, we found that the frequencies could lie within the operational range of the sensor but the turbulent kinetic energy had decreased by more than two orders of magnitude. This suggests minimal impact of the vortex shedding frequencies on the pressure measurement at the lower wind speeds.

To address flow separation over the probe's disks, we performed both analyses and flow visualization tests. The Reynolds number $Re = \rho u D / \mu$ on Mars based on the diameter (D) of the large disks is $< 4 \times 10^3$ for typical ambient wind speeds $u < 15$ m/s (Hess et al. 1977; Ryan et al. 1978; Murphy et al. 1990). When $\alpha = 0$ flow, separation over the disks is not expected to occur until $Re \gtrsim 10^5$. Hence, this scenario was found to be of no major concern. When $\alpha > 0$, N&B found in terrestrial flow experiments that $\varepsilon \equiv \Delta p / Q$, the error in their static pressure measurement relative to the dynamic pressure $Q = 1/2 \rho u^2$, was close to zero for a range of α but increased precipitously beyond some critical value we will term here α_{cr} . For example, at $u = 10$ m/s, they found that $\alpha_{cr} \approx 15^\circ$. Naturally, the question

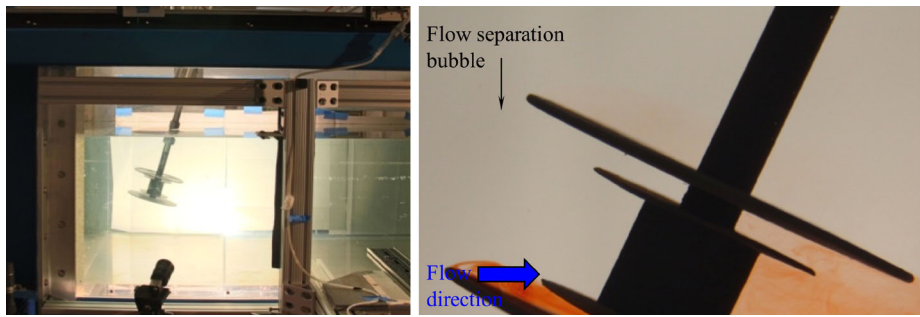


Fig. 17 Left: The test section of the Free Surface Water Tunnel at GALCIT used in the visualization of flow separation over the QD, at various angles of attack and for conditions similar to both Earth and Mars. Right: Typical result of dye recirculation in the flow separation bubble, emulating $Re = 6360$ on Mars at $\alpha = 25^\circ$

that arose for InSight was how this critical value would change on Mars considering that the Reynolds number is much lower there than during the terrestrial tests of N&B. It is already known from thin-airfoil tests that flow separates at smaller α when Re is reduced (McCullough 1955). This then implies that on Mars, α_{cr} for the QD could be lower than that determined in the terrestrial tests of N&B. To confirm these trends and to determine the favorable operational range of α for the QD on Mars, we performed flow visualization tests in the Free Surface Water Tunnel (FSWT) at the Graduate Aeronautical Laboratories of the California Institute of Technology (GALCIT) (Bobba 2004; LeHew 2012). The test section of this tunnel is 2 m long, 1 m wide and 0.56 m deep and is shown in Fig. 17, left, containing a model of the QD at an angle of attack. The FSWT is a recirculating shear layer facility with two streams that can be controlled independently. With the test section filled up to 56 cm by deionized water, the free-stream velocity can be varied (with no spurious oscillations) from 0.1–0.55 m/s. The test section is made of Lucite, with optical access from the bottom, top and sides of the test section.

Two distinct flow tests were performed in the FSWT. The first employed a model of the QD that was $1.2\times$ the size of that used by N&B. The objective was to validate our experimental approach (before employing it for Mars-related tests) by reproducing the value of $\alpha_{cr} \approx 15^\circ$ obtained by the authors in their wind tunnel tests at $u = 10$ m/s. At this speed, the Reynolds number was approximately 10^5 . This required a flow speed of ~ 0.5 m/s in the water tunnel to achieve flow similarity. The angle of attack was varied from 0 – 25° and a (red) dye was used over the lower large disk to visualize the characteristic separation bubble that is expected to occur when the flow over its edge separates. Because this feature of the separated flow involves flow recirculation inside the bubble, it is relatively easy to detect it with the dye, as shown by a typical test result in Fig. 17 (right). In this first test we found no separation at $\alpha < 10^\circ$ and clear separation at $\alpha > 18^\circ$. The transition to separation occurred between $12^\circ < \alpha < 16^\circ$, in agreement with the findings by N&B. The second flow test employed a $0.4\times$ -scale model of the QD to allow for similarity with flow conditions on Mars. The water flow speed was set to 0.1 m/s, representing $Re \approx 6 \times 10^3$ on Mars. This value is outside the expected range of $Re \sim 1500$ – 4000 for typical wind conditions, but not high enough to have a significant impact on α_{cr} . Our results support this conjecture since α_{cr} was found to be only about 1 – 2° lower than that produced by the terrestrial model at $Re \approx 10^5$. These tests therefore allowed us to determine the range of α within which we would expect the smallest errors associated with flow separation over the QD in our true static pressure measurements on Mars.

For winds with a low enough angle of attack and turbulent intensity, N&B report that the QD can reduce the wind-induced dynamic pressure effects by a factor of 100–10,000. For typical winds on Mars (e.g., 5.7 m/s) the un-filtered dynamic pressure effects are of order 0.36 Pa (well within our sensing capability, see below), but with the QD probe at the inlet of the pressure sensor, we can expect these perturbations to be reduced to about 3 mPa or below, well below our sensitivity. However, we were not able to empirically confirm this level of performance due to the very difficult nature of such a measurement. As noted above, before deployment, the WTS (Wind & Thermal Shield) will cover the Quad-Disk probe inlet for the PS, which will likely increase the Pressure Sensor's sensitivity to winds, but not invalidate the results entirely (i.e., likely < 0.36 Pa for 5.7 m/s winds).

The enclosed volume in the sensor, the inlet tubing and the QD probe between the atmosphere and the pressure sensor itself produces a response time (or alternatively a cutoff frequency) for the instrument as a whole. For perturbations shorter than this time, the sensor's response will be reduced. If we repeat the analysis above to determine the frequency dependent amplitude response of the full pressure sensor system (QD probe, inlet plumbing, sensor head space, not just the QD probe alone as above) we can determine a cutoff frequency of the first-order low-pass filter that this system represents. The cutoff frequency due to the complete inlet system of the pressure sensor is roughly 6 Hz. In addition to the mechanical filter of the plumbing, there is also a first-order low pass filter on the sensor electronics output with a cutoff frequency of about 3 Hz. The sensor output is read by an analog-to-digital converter on the PAE at 500 Hz, which is then averaged down to a 20 Hz data stream. The two cutoff frequencies in the system, along with the generally expected red spectrum of the pressure perturbations, provide adequate anti-aliasing filtering for the 10 Hz Nyquist frequency of the fundamental data rate of the pressure sensor.

4.2.2 Sensor Description

The InSight pressure sensor was produced by Tavis, which produced similar sensors that have flown and operated on the surface of Mars on the Viking and Pathfinder missions. Fundamentally, the sensor has a membrane separating an evacuated chamber from the inlet of the pressure sensor (which is open to the Mars environment). This membrane deflects as the ambient pressure changes. The deflection is measured using its varying impact on an electric circuit, in this case varying the reluctance of a circuit element associated with the membrane.

InSight's pressure sensor pushes the limits of capabilities of pressure sensors that have previously flown to Mars' surface. InSight's pressure sensor shares the Tavis design heritage with the Viking and Pathfinder lander pressure sensors in that all are variable reluctance sensors. The essential difference with the InSight instrument is that, from the ground up, the electronics were designed to have the lowest noise floor possible in a flight qualified electronics package. A large contributor to the overall noise budget for low frequency applications is so-called $1/f$ noise. This is low frequency noise for which the noise power is inversely proportional to the frequency with a typical bandwidth of approximately 0.01 to 10 Hz, spanning the range of frequencies of interest to InSight. The components used in the electronics package for InSight had the lowest possible noise found in flight-qualified parts.

The Tavis pressure sensor uses a form of synchronous chopped demodulation. This scheme has been used in all Tavis spaceflight hardware prior to InSight, and was considered for InSight. However, it was seen early on that this topology would not be sufficient for InSight. Early tests indicated that the noise limit of the heritage circuits was 2.5 times higher than the specification would allow. Chopped demodulation techniques can have some

low frequency noise issues due to the switching noise associated with discrete electronics. Chopped demodulation can introduce switching artifacts that contain harmonics that are injected into the signal chain and are very hard to filter out. Noise at each harmonic is demodulated back to dc along with the signal being measured.

Because of the aforementioned switching noise, Tavis elected to use an absolute value form of synchronous sine wave demodulation. This approach is much less susceptible to noise and can recover very small signals in the presence of large noise or interference. Low noise design concepts were developed for the sensing elements as well. These techniques were employed to control the dimensionally-driven impedance variability seen in discrete wiring that may have been introduced into the sensor signal chain by ground tilt and vibration. We were able to demonstrate a noise floor of 1 to 10 μV dc for the electronics package apart from the gage element. The ultimate noise floor of the overall sensor is driven by a fundamental aspect of the gage element itself, but its cause is still under investigation.

It was anticipated that the pressure sensor's membrane's behavior would be temperature-dependent. To minimize temperature variations on the sensor, it was located within the lander body. Additionally, the electronics were assembled using components with minimal thermal sensitivity. Nevertheless, the sensor was also provided with a temperature sensor near the membrane to allow calibration to account for the inevitable temperature changes that the sensor will undergo.

4.2.3 Calibration & Drift

A test chamber was built at JPL that enabled holding the sensor at a specified temperature (spanning the range of expected flight temperatures), and exposing the sensor's inlet to a variable pressure (again, spanning the range of expected ambient pressures at the landing site throughout a full Mars year). The pressure of the test chamber was monitored by a second pressure sensor, traceable to NIST standards, and with a precision and accuracy similar to that of InSight's pressure sensor. In addition to slow changes in the test chamber pressure, a variable frequency oscillating plunger system was connected to the chamber to allow sinusoidal pressure fluctuations of known amplitude and frequency to be imposed on the system. This test chamber was used to not only establish the calibration of the sensor, but to also demonstrate that it met the noise floor requirements, and to produce a transfer function versus frequency for the system as a whole. Unfortunately, the oscillating plunger system was unreliable above 1 Hz, so the mechanical cutoffs of the system plumbing could not be empirically verified in the test setup, and analytical estimates are all that exist to produce the estimate discussed above.

The noise spectrum of the pressure sensor is the principal requirement it had to pass. This was measured in the test setup by maintaining the chamber at a constant pressure, and monitoring the spectrum of the noise on the pressure sensor's output. A representative example of this is shown in Fig. 18, with the actual time series on the left and the resultant power spectrum on the right. The blue line on the figure represents the noise floor requirement established to be of value in removing pressure-induced noise on the SEIS sensor readings. The noise spectrum of the signal from the pressure sensor is shown in red and is below the noise floor requirement at all frequencies of interest (i.e., 0.01–1 Hz). This type of test was conducted at each of a set of temperatures spanning the operational range of the instrument, and in all cases, the noise spectrum was below the requirement, although the noise amplitude shifted up and down slightly with temperature. The typical RMS variability of the sensor when reading under constant pressure conditions is of the order of 10 mPa.

The sensor is designed to measure between pressures of about 550 Pa and 1000 Pa, exceeding the expected range of the pressure extremes that will be experienced at the InSight

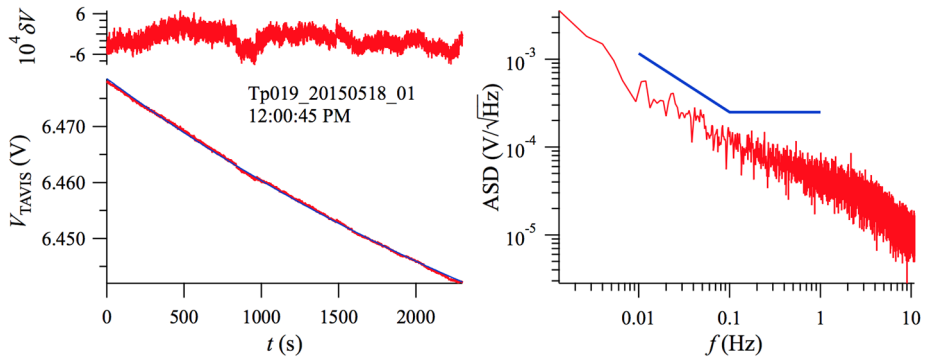


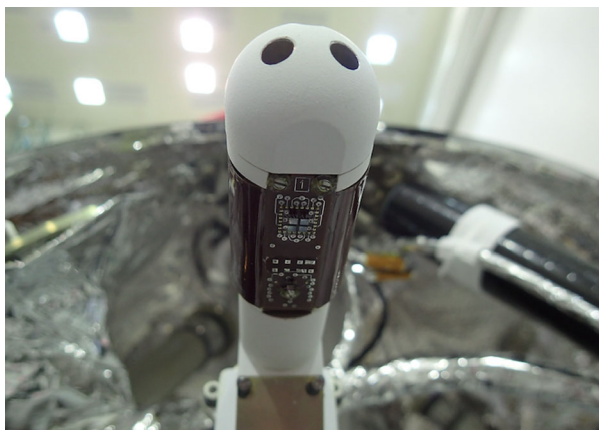
Fig. 18 (Left) Representative time series during about 2300 s of relatively steady (although decreasing) pressure. The lower plot is the actual voltage output from the sensor, while the upper plot is the de-trended version of the same data. The typical RMS of the time series translates to of order 10 mPa when converted to pressure. (Right) The power spectrum of that same time series is shown in red. The mission requirements for the noise floor of the pressure sensor is shown as the blue lines from 0.01–1 Hz. In all cases, the instrument noise is below the requirement

landing site (see Sect. 3.2), and for temperatures between -30°C and 40°C . The actual calibration is temperature-dependent, so the ultimate range possible for the instrument will depend on the thermal environment realized. The sensor was actually calibrated twice, owing to the 26-month delay between the originally planned launch date (2016) and the actual launch date in 2018. The first calibration was in April and May, 2015, and the second calibration was done in May, 2017. The latter calibration will be used in flight operation of the sensor, but the expected drift can be assessed by changes in the calibration between the two years. In each of the calibration procedures, the sensor was held near a particular temperature, and the chamber pressure was varied in a series of ~ 25 steps, starting at ~ 550 Pa and going up to about 1000 Pa, and then stepping back down (to assess hysteresis) over a total time of about 2 hours. This pressure cycling was then repeated at a different temperature for the sensor after waiting a suitable equilibration time for the system to adjust to the new temperature (several hours). Overall, 14 temperatures were used to cover the pressure/temperature operating space of the pressure sensor and produce empirical fits to the measured pressure as a function of the sensor output voltage and the sensor temperature.

At each pressure step for a particular sensor temperature, data were taken for about 5 minutes while the system equilibrated. The data taken during the transients were removed, and only those from steady conditions were used. This resulted in a set of $14 \times 25 = 350$ discrete combinations of temperature and pressure that could be used to develop a functional form relating the sensor's output voltage and its temperature to the actual pressure it was exposed to. We experimented with formulas of increasing complexity, and found that a third order polynomial in both the measured voltage and temperature could explain the majority of the variability seen in the calibration process without introducing extra noise in the results. Using the optimized cubic fit in sensor voltage and temperature to estimate the actual pressure on the sensor results in a typical absolute error of about 1.5 Pa. While absolute accuracy is not a requirement on the InSight pressure sensor, it is relevant for the ancillary science discussed in Sect. 2.2 above.

We were able to compare the first calibration process to the second, to see how a 2-year span could change the absolute calibration of the sensor. For a broad cross-section of temperatures and pressures, the typical difference between the best fit pressure estimate from

Fig. 19 Details of TWINS' Wind Sensor. View of the bottom board, with the four dice at the close tip, and the cold die at the far end



the 2015 calibration and the 2017 calibration ranges from 0 to ~ 1.5 Pa. This is roughly a 0.06% drift over a period of about 1 Mars year. Viking saw a drift of about 0.07% over 2 Mars years (Haberle and Kahre 2010). While this indicates that the absolute calibration of the InSight pressure sensor is not as stable as those on the Viking Landers, it should still provide sufficient accuracy to enable a study on secular change in the atmospheric pressure, as discussed in Haberle and Kahre (2010).

4.3 TWINS

4.3.1 Sensor Description

TWINS (Temperature and Winds for InSight) comprises two identical horizontal booms arrayed with wind and temperature sensors placed on diametrically opposite sides of the lander deck, as shown in Fig. 4. The booms are attached to a supporting structure, approximately 1.6 m above the ground level, 265 mm above the lander top deck (on top of a pair of brackets), horizontally placed, and in parallel with respect to each other, but facing away from each other. These are at approximately the $+Y$ and $-Y$ sub-axis of the lander.

This layout is intended to minimize the perturbing effects on the wind flow induced by the other elements in the lander top deck, by ensuring that at least one of the booms will record relatively clean, unperturbed wind data for any given wind direction.

The tip of each boom is shrouded with three sensor boards (bi-dimensional hot film anemometers), each containing four hot dice which are heated and exposed to the airflow, and a fifth cold die used for reference (Figs. 19 & 20). These three boards, jointly, comprise the 3D wind sensor on each boom.

These two 3D wind sensors, one per boom, use thermal anemometry to record the wind speed and direction. The concept behind the hot film anemometry is based on recording the amount of power required to heat the hot dice (a thin titanium film resistor patterned on the surface of a silicon chip (Dominguez et al. 2008) so that it maintains a constant temperature difference with respect to the ambient temperature as measured by the cold die). From that, the convective power is estimated and, in turn the wind speed and direction is calculated by differencing measurements between hot and cold detectors, and between sensor boards facing in different directions.

Additionally, a sensor extending below each boom provides air temperature measurements. It is a 35 mm long thin fin, manufactured with a multilayer of FR4 (a glass reinforced

Fig. 20 One of the TWINS wind sensors, showing two of the boards. Each boom has three identical boards, connected to the ASIC that is placed in the base of the boom. The boards have four hot dice at the tip (with three resistors printed on the upper side of a silicon chip—a resistor for heating, another for measuring the temperature, and the third one to be used as a reference sensor in the measurement circuit), and one cold die at the base (having only a resistor that is used as a temperature reference)

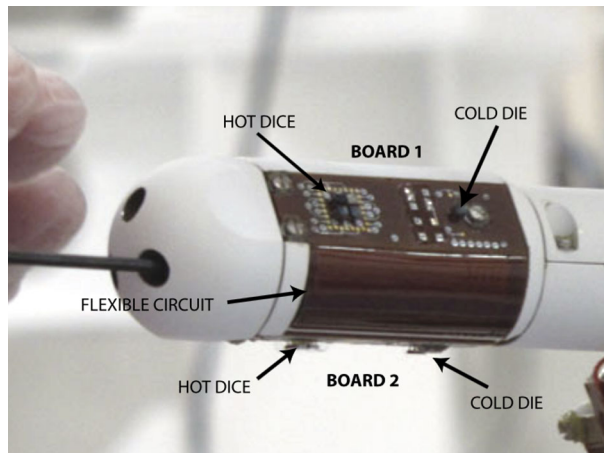
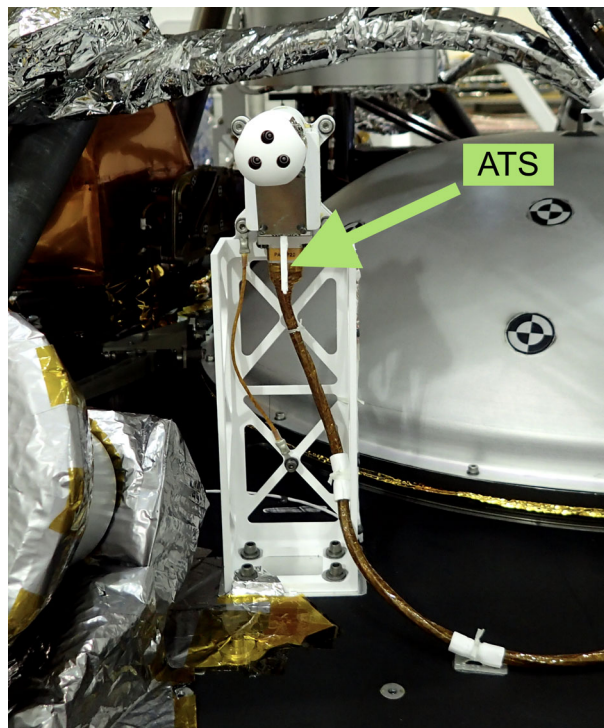


Fig. 21 Details of one of the TWINS' booms (attached to its supporting structure that raises it over the surrounding elements). The Air Temperature Sensor rod is also shown (indicated by the green arrow), attached to the base of the boom



epoxy laminate material, a very low thermal conductivity material), and with two mini-sens RTD thermistors (PT1000 Class A type, and 2.3 mm × 1.6 mm in size) (see Figs. 21 & 23). The two thermistors are bonded to the tip and at an intermediate position in the rod. Additionally, a third thermistor at the rod base is also used to monitor the boom temperature. Data from these three thermistors are used to estimate the temperature of the fluid around the instrument, despite the thermal contamination from the boom.

Fig. 22 Example of flow perturbations by the lander and on-deck elements. The turbulent regime is highly dependent on the surrounding elements. Specific calibration campaigns or, in their absence, exhaustive and detailed CFD simulations and analysis, are mandatory to fully understand the undisturbed ambient wind given the observed winds at each TWINS boom

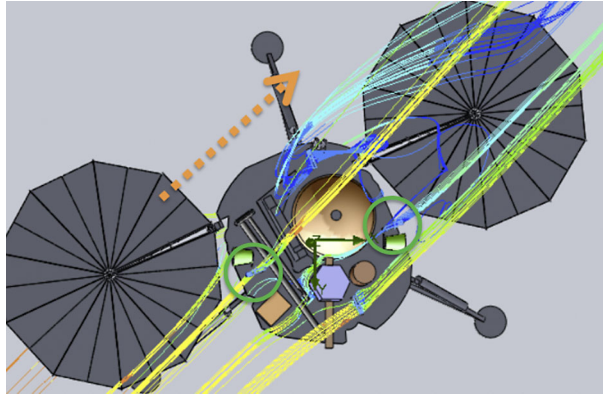
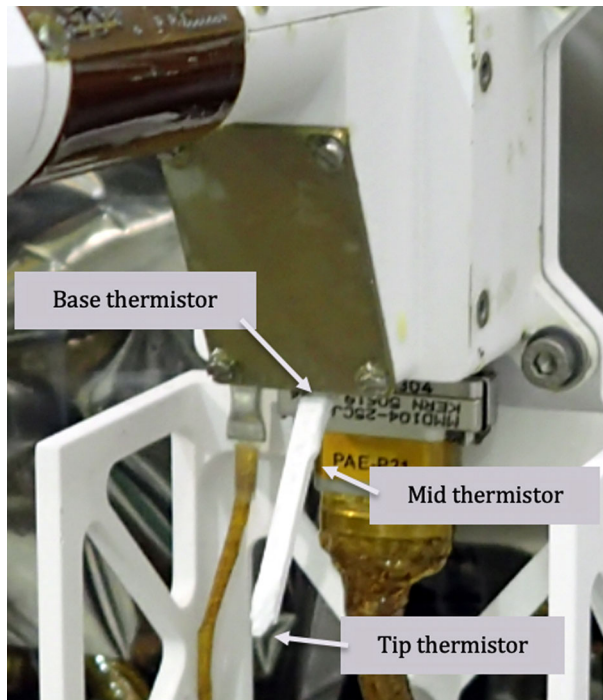


Fig. 23 Image of Atmospheric Temperature Sensor (ATS) rod. Each ATS is a multilayer FR4 rod, 35 mm long, with two PT1000 Class A thermistors (at the tip, and in an intermediate position)



TWINS Electronics Two front-end mixed-signal ASICs, one per boom, process all of the received analog inputs from the transducers and send the data to the PAE via a serial communication link. The ASICs implement individual electro-thermal sigma-delta control loops for each die, driving power to each of the hot dice in the boards, with the goal of keeping each hot dice at a fixed temperature difference with respect to the cold die in each board. The front-end ASICs are each furnished with a heater to be able to warm-up the ASICs to any given operational temperature, as far as needed, by means of a heater power line. That power line is regulated externally by the PAE using an ASIC temperature thermistor read-out also provided in the interface. The target operational temperature, known as the heater setpoint, is configured from the ground. Additionally, the TWINS' ASICs also implement the analog-

to-digital converters to sample the air temperature sensors' PT1000, sending those data to the PAE.

The TWINS booms are controlled and configured via several configuration registers (ASIC Registers) which are, in general, used to enable/disable operation (temperature or wind acquisitions), to configure the internal analogue acquisition chain (multiplexer, filter, ADC and amplifier gains) to define several operational engineering parameters (band gap reference level and compensation resistor parameters), for configuring the wind sensor heating and measurement currents, and for supporting internal ASIC development and characterization tests. The state of all of these configuration registers must be uploaded to the TWINS booms after each boom is powered on.

4.3.2 Estimation of Free-Stream Winds

The TWINS booms are relatively close to InSight's deck, as well as to the other structures also on the deck. Thus, wind and temperature readings will be strongly influenced by the lander platform, as has been confirmed by CFD simulations. In such a context, the retrieval of wind and temperature magnitudes requires not only using the calibration values and coefficients to yield the wind in the immediate vicinity of the booms, but also CFD simulations to put these locally measured winds in context of the perturbations from the other items on the deck, particularly during the first sols, when all the instruments will be on top of the lander prior to deployment.

Flows around a cylindrical shape have been studied extensively in aerodynamics. It is generally understood that when a fluid flows around a cylinder, there is a zone where the stream is detached, and another in which the fluid follows the shape of the body, having a stagnation point in the point of impact. This is the underlying idea behind the TWINS wind sensor cylindrical design. It is also known that the flow very close to the boom surface is almost two-dimensional, with the normal component being negligible. The velocity field in the vicinity of the surface of a cylindrical body is a function of the fluid properties, the geometry of the flow, and the free flow speed. In particular, for the flow around a semi-infinite cylinder, it can be written:

$$V/U_{\infty} = F(Re, \theta, \phi, r/D, d/D) \quad (5)$$

where V is the local speed, U_{∞} is the speed of the free flow, Re is the Reynolds number, θ and ϕ the incident and azimuth angles, D is the cylinder diameter, r the radial distance from the cylinder axis to the point under study, and d is the distance from the point to the end of the boom (details are provided in Gomez-Elvira et al. 2012).

As in the case of the REMS wind sensor on the Curiosity rover, the TWINS wind sensors are designed to estimate U_{∞} , θ and ϕ on the basis of two estimators of the local speed components at three points close to the cylinder surface. This is further based on the fact that with three measurement points arranged every 120° around the circumference of each boom, at least two of them will be outside the flow separation region for most wind incidence angles.

In summary, all these considerations led to design the REMS and TWINS booms as a set of three 2D wind speed sensors that record the local 2D winds apparent on the surface of the booms at their various position angles. The combined reading from all three of those boards in each boom will enable the wind speed and direction that each boom experiences to be determined.

To retrieve the 2D wind magnitudes, the first step is to determine the thermal conductance of each die, computing the *longitudinal* (two front dice minus the two back ones),

and *transversal* (two left dice minus two right ones) differential conductances. These are referred to as the G_{long} and G_{trans} conductances. They are both proportional to the Nusselt number, and therefore directly related to the local wind speed (Dominguez et al. 2008).

To estimate the thermal conductance of each die requires estimating the convection power emitted by each die. At thermal equilibrium, the power injected into each die equals the conductive and radiative power losses, plus the power lost by convection to the ambient air. These losses can be estimated from the conductive and radiative constants from empirical sensor calibration tests.

$$G = \frac{P_{\text{convec}}}{T_{\text{hot}} - T_{\text{air}}} = \frac{P_{\text{delivered}} - P_{\text{conduction loss}} - P_{\text{radiation}}}{T_{\text{hot}} - T_{\text{air}}} = hA \quad (6)$$

$$h = Nu \frac{k}{l} = g(Re, Pr) \frac{k}{l}$$

where A is the dice surface area, k is CO_2 thermal conductivity, l is the characteristic die dimension, Pr is the Prandtl number of the fluid, and Re and Nu are the Reynolds and Nusselt numbers for that fluid and speed.

With the ambient temperature and pressure, it is possible to compute the fluid properties *locally* at each boom level, stating the relation between G and Re , and therefore, between G and $(U_{\infty}, \theta, \phi)$, given by

$$Re = K \cdot P \cdot U_{\infty} \quad (7)$$

where K is a coefficient which is a function of the fluid characteristics, and P is the pressure.

Through an extensive testing campaign at the CAB linear wind calibration facility, the team has generated a dense look-up-table that relates pitch and yaw angles, and Reynolds numbers (wind speed), with the two G components of the boards in the boom under test. An inverse retrieval algorithm has been developed, where the pitch, yaw and Reynolds number values are identified that minimize the difference between the values in the look-up table and those measured by the sensor. This yields the local wind speed and direction at the boom in consideration.

However, the $(U_{\infty}, \theta, \phi)$ *locally* estimated for each operating boom may substantially differ from one another, and also from the *global* free-stream $(U_{\infty}, \theta, \phi)$ due to the perturbations caused by the lander and the elements near each boom. Because of this, to estimate the true, unperturbed free-stream wind speed and direction, we also rely on CFD simulations (see Fig. 22). These simulations have been run at representative “average” Elysium Planitia conditions, using a detailed model of the lander with (and without) the elements on top of the deck, and covering a full mesh of possible wind speeds and incident angles. For each yaw and pitch of the simulation mesh, the wind speed correction curve as a consequence of the presence of the lander, and with respect to the free-stream wind, is estimated for several free flow speeds. This correction factor is then used to estimate the unperturbed free flow speed from the lander-perturbed wind readings.

4.3.3 Estimation of the Ambient Temperature

The TWINS air temperature sensor is used to estimate a temperature representative of the local environment, even in the presence of thermal perturbations from the lander and/or solar panels and direct solar illumination. Ground data processing attempts to minimize these contaminating effects.

The retrieval model used to estimate the ambient temperature makes use of the readings provided by the three thermistors on each rod (see Fig. 23): at the base, at the intermediate

position, and at the tip. With these three thermistors, the temperature profile on the rod, and the local air temperature can be estimated. The TWINS temperature sensor's retrieval model is similar to that of REMS, and is based on the physics of a thin fin in thermal balance with the fluid around it. The model is detailed in Zorzano et al. (2009), and has been experimentally validated by Mueller and Abu-Mulaweh (2006). In both the REMS and TWINS cases, and as it is described in those works, the temperature profile on the rod depends on the conduction through the FR4 material and the wires, the local convection (natural and forced) within the Martian atmosphere, the IR radiative interchange between the rod and the surrounding air mass, and the solar radiative heating as the most significant terms.

The retrieval algorithm provides the temperature of the surrounding fluid on the bases of the three known temperatures (thermistors on the rod), the local convection and radiation terms, and design parameters of the rod (conductivity, length, emissivity, etc.). This mathematical model has been validated through experimental tests in Martian simulation chambers.

4.3.4 Differences from REMS

TWINS has a high level of heritage from the REMS wind and temperature sensor booms from the Curiosity rover. The overall design of four heated dice and one cold die, arranged with three sets around the tip of a cylindrical boom is maintained. Using two booms to avoid problems with wind azimuths where any one boom performs poorly is also retained. The retrieval algorithms for each boom's local wind as well as that for the air temperature sensors are also inherited from REMS. However, some significant improvements in the TWINS booms have been incorporated using lessons learned from REMS.

The PAE can automatically change parameters for the boom operation instead of having them be manually controlled by instrument operators on the ground. This should result in better fidelity data, with the booms operating with the appropriate set of parameters most of the time. The PAE can also better control the ASIC voltage, as well as their operating temperature, through direct control of the heater. This too should substantially increase the usable fraction of TWINS data versus that of REMS. Finally, the TWINS flight models were themselves fully characterized in the calibration process, not an indirect calibration with a stand-in, as was done with REMS. This should result in significantly smaller residuals in fitting between the wind vector look-up tables and the actual measurements, increasing confidence, accuracy and precision of the results.

5 Instrument Operations

In general, the APSS sensors will be operated nearly continuously throughout the mission (as power availability permits), and their data will be stored in a circular memory buffer on the spacecraft with a duration of roughly 5 weeks before being overwritten by new data. APSS operations will be made in coordination with those of the SEIS instrument by the SEIS operation center SISMOC, in close coordination with JPL and the APSS Instrument teams. Detailed description of SISMOC can be found in Lognonné et al. (2018). Because of downlink limitations, only a fraction of the total data from the APSS sensors can be returned to Earth. To intelligently manage the disconnect between observed and downlinked data, the spacecraft downlinks a sub-sampled version of the continuous data stream, as well as an estimate of the power contained at frequencies above the down-sampling frequency for IFG

and PS. Using these continuous (but low data rate) time series from the APSS sensors, the science team can selectively choose subsets of the data for downlink at the full (or at least increased) data sampling rate. At the nominal total downlink of ~ 38 Mbits per sol, this allows roughly 30 minutes per sol of full data rate downlink of all APSS sensors after the low data rate continuous data is accounted for.

5.1 Insight FluxGate

The magnetometer can be in either one of two states: operating or non-operating. However, as discussed above, the output from the magnetometer can be averaged to lower rates to match telemetry allocations or the needs of the SEIS investigation. For the nominal case (~ 38 Mbits per sol), the IFG returns data down-sampled to 0.2 Hz with its temperature data sampled at 0.02 Hz. On-board processing calculates the total power in the three components of the magnetic signal above 0.1 Hz, which is down-sampled and returned to Earth. This is expected to be used to identify events for which downlink of the full 20 Hz data is desired.

5.2 Pressure Sensor

As with the IFG, the pressure sensor is either operating or non-operating. The native sampling rate on board the lander is 20 Hz, although on-board processing will downsample this to a lower sampling rate continuous data stream. For the nominal downlink case, the pressure sensor will return continuous data down-sampled to 2 Hz, and its temperature sensor data will be down-sampled to 0.2 Hz. Onboard processing will also produce the RMS of a high-pass version of the pressure signal above 1 Hz, which will be down-sampled to 0.5 Hz. This latter signal is indicative of high frequency pressure variations above that resolved in the continuous pressure data, to focus attention for downlink of the full sampling rate data in an “event.”

5.3 TWINS

TWINS operation is designed around two main phases:

1. Deployment phase.
2. Science monitoring phase.

During deployment phase, TWINS aim is to provide data regarding wind, with the objective of assessing when to deploy instruments. During that phase, it is expected that both booms will be used at the same time, although this will depend on available resources (such as power and bandwidth). Data from both booms will be used on the ground to retrieve wind speed and direction, as well as air temperature. Having both booms operating during this first phase will maximize the record of unperturbed winds.

During the science monitoring phase, after all instruments (SEIS, WTS, HP3) are deployed, the nominal plan is to have only one boom operating at any one time, with provisions to switch booms several times a day. The exact times for these boom switches will be modified on a weekly basis as the seasons progress, based on the previous week’s data, with the goal of always operating with the boom that is predominantly upwind of the lander for any given wind direction expected at a given time of day. If power allows, both booms may be operated to yield a more robust wind estimate in the presence of quickly varying wind directions due to turbulent winds in the convective boundary layer. Having the two booms pointed in opposite directions simultaneously operating will allow the team to get accurate

measurements of the wind's diurnal and seasonal tendencies, which in turn will be used to decide which boom to have on at different times during operations when only one boom is nominally powered. Having both booms operating simultaneously is the preferred configuration, although having just one is a compromise solution in case of restricted resources.

In both mission phases, continuous logging is the main driver for TWINS operation, based on the Payload Auxiliary Electronics' capability of measuring without interruption and autonomously from the lander computers. TWINS collects data at 1 Hz, but as with IFG and PS, TWINS also sends back down-sampled continuous data in addition to the selected 'event' data at higher sampling rate. For all TWINS data, a decimation rate is applied. Under nominal conditions we expect to send back TWINS wind data at 0.1 Hz continuously. For TWINS Air Temperature data, a 10 s average and standard deviation is computed on board for continuous downlink also at 0.1 Hz.

5.4 PDS and IRIS/MSDS Submission

The data from APSS will be archived with the Planetary Data System in two separate nodes. Specifically, the IFG data will be archived with the Fields and Particles Node at UCLA, and the TWINS and Pressure Sensor data will be archived with the Atmospheres Node at New Mexico State University. In both cases, the archives will include the raw data from the various sensors as they come from the spacecraft. They will also include calibrated data (in physical units) after applying the calibration functions. In the case of IFG, this means the 3-D magnetic field vector time series. For PS & TWINS, this means the pressure, and the pressure sensor's temperature, and the wind speed, wind direction and air temperature for each boom. Finally, for the TWINS data, we will also archive an estimate of the ambient wind (speed and direction) and air temperature that would exist without any of the perturbations from the lander itself.

In addition and because of their importance for seismological analysis, all APSS data will be also deposited in the Mars SEIS data System in IPGP and in the IRIS Data Management Center. The format of the APSS data will be SEED. See Lognonné et al. (2018) for more detail and information.

6 Summary

The APSS environmental sensor suite provides the capability to remove the significant potential environmental contaminating influences on InSight's SEIS sensors' readings. The APSS sensors were selected to provide measurements of magnetic field, atmospheric pressure, wind speed and direction and air temperature at levels of precision and sampling rate needed to serve as critical auxiliary data in support of the seismometry on InSight. Additionally, they will also enable fundamental studies of the Martian surface magnetic field and boundary layer atmospheric dynamics.

The magnetometer has been properly tested and well accommodated. The sensor will monitor the AC magnetic field of the spacecraft and any environmental magnetic signals. This will allow separation of natural seismic signal from magnetic influences. The magnetometer should also provide measurements of low-frequency induction signals associated with the solar wind interaction, possibly Martian atmospheric phenomena, and we expect to detect induced currents from the Martian core.

The pressure sensor is the most sensitive yet flown to Mars. Its accommodation on the lander should yield an excellent measure of the ambient pressure, with the sensor itself inside

the thermally moderated body of the lander, and the inlet using a specially modified Quad-Disk probe to minimize wind-induced dynamical pressure effects. The greater sensitivity of the pressure sensor will allow a dust devil census to extend to significantly greater range from the lander, and the high precision and frequency response may reveal infrasound in the Martian atmosphere.

The TWINS booms are an improved version of the flown wind and air temperature sensors from REMS on the Curiosity Rover. The technical improvements in the sensors, as well as better accommodation on the lander, should yield a valuable data set to identify true seismic events from those due to wind-induced shaking. The continuous winds that will be available from InSight will be a first at Mars, and may finally enable direct determination of the Aeolian threshold wind speed on Mars.

Acknowledgements The work reported here on the IFG was supported by NASA/JPL under contract 1521593. We are grateful to Hannes Leinweber for his assistance with the testing of the magnetometer.

SISMOC center is supported by the French Space Agency CNES. We thank David Mimoun for his work developing and clarifying the APSS sensor requirements as they flow-down from SEIS requirements.

Concerning TWINS, the authors thank the Centro de Desarrollo Tecnológico e Industrial (CDTI), Ministerio de Economía y Competitividad (ESP2013-43503-R, ESP2014-54256-C4-1-R, ESP2015-68281-C4-1-R and ESP2016-79612-C3-1-R) and the Instituto Nacional de Técnica Aeroespacial (INTA) of Spain for funding this project, and to CRISA (an Airbus Defence and Space Company) for the technological involvement in the project.

This is InSight contribution number 50.

References

- M.H. Acuna, J.E.P. Connerney, N.F. Ness et al., *Science* **284**, 790–793 (1999)
- R. Beauduin, P. Lognonné, J.P. Montagner, S. Cacho, J.F. Karczewski, M. Morand, *Bull. Seismol. Soc. Am.* **86**, 1760–1769 (1996)
- K.M. Bobba, *Robust Flow Stability: Theory, Computations and Experiments in Near Wall Turbulence* (California Institute of Technology, Pasadena, 2004)
- P. Bradshaw, D.G. Goodman, *The Effects of Turbulence on Static Pressure Tubes*. (Her Majesty's Stationery Office, London, 1968)
- T. Christiansen, P. Bradshaw, *J. Phys. E, Sci. Instrum.* **14**, 992–997 (1981)
- J.E.P. Connerney, J. Espley, P. Lawton, S. Murphy, J. Odom, R. Oliverson, D. Sheppard, *Space Sci. Rev.* **194**, 257–291 (2015)
- S.S. Dolginov, *Geophys. Res. Lett.* **5**, 89–92 (1978a)
- S.S. Dolginov, *Kosm. Issled.* **16**, 257–268 (1978b)
- S.S. Dolginov, Y.G. Yeroshenko, L.N. Zhuzgov, *J. Geophys. Res.* **81**, 3353–3362 (1976)
- M. Dominguez, V. Jimenez, J. Ricart, L. Kowalski, J. Torres, S. Navarro, J. Romeral, L. Castanet, *Planet. Space Sci.* **56**, 1169–1179 (2008)
- T. Forbriger, R. Widmer-Schmidrig, E. Wielandt, M. Hayman, N. Ackerley, *Geophys. J. Int.* **183**(1), 303–312 (2010). <https://doi.org/10.1111/j.1365-246X.2010.04719.x>
- R.F. Garcia, Q. Brissard, L. Rolland, R. Martin, D. Komatitsch, A. Spiga, P. Lognonné, B. Banerdt, *Space Sci. Rev.* **211**, 547–570 (2017)
- M. Golombek, M. Grott, G. Kargl, J. Andrade, J. Marshall, N. Warner, N.A. Teanby, V. Ansan, E. Hauber, J. Voigt, R. Lichtenheldt, B. Knapmeyer-Endrun, I.J. Daubar, D. Kipp, N. Muller, P. Lognonné, C. Schmelzbach, D. Banfield, A. Trebi-Ollennu, J. Maki, S. Kedar, D. Mimoun, N. Murdoch, S. Piqueux, P. Delage, W.T. Pike, C. Charalambous, R. Lorenz, L. Fayon, A. Lucas, S. Rodriguez, P. Morgan, A. Spiga, M. Panning, T. Spohn, S. Smrekar, T. Gudkova, R. Garcia, D. Giardini, U. Christense, T. Nicollier, D. Sollberger, J. Robertsson, K. Ali, B. Kenda, W.B. Banerdt, *Space Sci. Rev.* (2018). <https://doi.org/10.1007/s11214-018-051207>
- J. Gomez-Elvira, C. Armiens, L. Castaner, M. Dominguez, M. Genzer, F. Gomez, R. Haberle, A.-M. Harri, V. Jimenez, H. Kahanpaa, L. Kowalski, A. Lepinette, J. Martina, J. Martin-Frias, I. Mcewan, L. Mora, J. Moreno, S. Navarro, M.A. de Pablo, V. Peinado, A. Pena, J. Polkko, M. Ramos, N.O. Renno, J. Ricart, M. Richardson, J. Rodriguez-Manfredi, J. Romeral, E. Sebastian, J. Serrano, M. de la Torre Juarez, J. Torres, F. Torrero, R. Urqui, L. Vazquez, T. Velasco, J. Verdasco, M.-P. Zorzano, J. Martin-Torres, *Space Sci. Rev.* **170**, 583–640 (2012)

- R.A. Gurnett, D.D. Morgan, L.J. Granroth, B.A. Cantor, W.M. Farrell, J.R. Espley, *Geophys. Res. Lett.* **37**, L17802 (2010)
- R.M. Haberle, M.A. Kahre, *Mars* **5**, 68–75 (2010). <https://doi.org/10.1555/mars.2010.0003>
- R.M. Haberle, M. de la Torre Juarez, M. Kahre, D.M. Kass, J.R. Barnes, J.L. Hollingsworth, A.-M. Harri, H. Kahanpaa, *Icarus* **307**, 150–160 (2018)
- S.L. Hess, R.M. Henry, C.B. Leovy, J.A. Ryan, J.E. Tillman, *Trans. Am. Geophys. Union* **58**, 827 (1977)
- J.P. Holman, W.J. Gajda, *Experimental Methods for Engineers*, 3rd edn. (McGraw-Hill, New York, 1978)
- B. Kenda, P. Lognonné, A. Spiga, T. Kawamura, S. Kedar, W.B. Banerdt, R. Lorenz, D. Banfield, M. Golombek, *Space Sci. Rev.* **211**, 501–524 (2017)
- F. Kuhnke, M. Menvielle, G. Musmann, J.F. Karczewski, H. Kügler, C. Cavot, P. Schibler, *Planet. Space Sci.* **46**(6–7), 749–767 (1998). [https://doi.org/10.1016/S0032-0633\(98\)00010-5](https://doi.org/10.1016/S0032-0633(98)00010-5)
- B. Langlais, M.E. Purucker, M. Manda, J. Geophys. Res., Planets **109**(E2), E02008 (2004)
- B. Langlais, F. Civet, E. Thébaud, J. Geophys. Res., Planets **122**(1), 110–123 (2017)
- J.A. LeHew, *Spatio-Temporal Analysis of the Turbulent Boundary Layer and an Investigation of the Effects of Periodic Disturbances* (California Institute of Technology, Pasadena, 2012)
- P. Lognonné et al., *Space Sci. Rev.* (2018, submitted)
- P. Lognonné, B. Mosser, *Surv. Geophys.* **14**(3), 239–302 (1993)
- P. Lognonné, V.N. Zharkov, J.F. Karczewski, M. Romanowicz, M. Menvielle, G. Poupinet, B. Brient, C. Cavoit, A. Desautz, B. Dole, D. Franqueville, J. Gagnepain-Beyneix, H. Richard, P. Schibler, N. Striebig, *Planet. Space Sci.* **46**(6–7), 739–747 (1998). [https://doi.org/10.1016/S0032-0633\(98\)00009-9](https://doi.org/10.1016/S0032-0633(98)00009-9)
- R.D. Lorenz, S. Kedar, N. Murdoch, P. Lognonné, T. Kawamura, D. Mimoun, W.B. Banerdt, *Bull. Seismol. Soc. Am.* **105**, 3015–3023 (2015)
- W.J. Massman, R.A. Sommerfeld, A.R. Mosier, K.F. Zeller, T.J. Hehn, S.G. Rochelle, *J. Geophys. Res.* **102**(D15), 18851–18863 (1997)
- G.B. McCullough, The effect of Reynolds number on the stalling characteristics and pressure distributions of four moderately thin airfoil sections, NACA Technical Note 3524. Ames Aeronautical Laboratory, Moffett Field, CA (1955)
- D. Mimoun, N. Murdoch, P. Lognonné, K. Hurst, W.T. Pike, J. Hurley, T. Nebut, W.B. Banerdt (SEIS Team), *Space Sci. Rev.* **211**, 383–428 (2017)
- A. Mittelholz, C.L. Johnson, R.J. Lillis, *J. Geophys. Res., Planets* **122**(6), 1243–1257 (2017)
- A. Mittelholz, C.L. Johnson, A. Morschhauser, *Geophys. Res. Lett.* **45**, 5899–5907 (2018)
- A. Morschhauser, V. Lesur, M. Grott, *J. Geophys. Res., Planets* **119**(6), 1162–1188 (2014)
- D.W. Mueller Jr., H.I. Abu-Mulaweh, *Appl. Therm. Eng.* **26**, 1662–1668 (2006)
- N. Murdoch, B. Kenda, T. Kawamura, A. Spiga, P. Lognonné, D. Mimoun, W.B. Banerdt, *Space Sci. Rev.* **211**, 501–524 (2017)
- J.R. Murphy, C.B. Leovy, J.E. Tillman, *J. Geophys. Res.* **95**, 14555–14576 (1990)
- K. Nishida, Y. Fufao, S. Watada, N. Kobayashi, M. Tahira, N. Suda, K. Nawa, T. Oi, T. Kitajima, *Geophys. J. Int.* **162**(3), 824–840 (2005)
- R.T. Nishiyama, A.J. Bedard, *Rev. Sci. Instrum.* **62**, 2193–2204 (1991)
- C.T. Russell, *Geophys. Res. Lett.* **5**, 85–88 (1978)
- C.T. Russell, *Phys. Earth Planet. Inter.* **20**, 237–246 (1979)
- C.T. Russell, R.C. Elphic, J.A. Slavin, *J. Geophys. Res.* **85**, 8319–8332 (1980)
- C.T. Russell, B.J. Anderson, W. Baumjohann, K.R. Bromund, D. Dearborn, D. Fischer, G. Le, H. Leinweber, D. Leneman, W. Magnes, J.D. Means, M.B. Moldwin, R. Nakamura, D. Pierce, F. Plaschke, K.M. Rowe, J.A. Slavin, R.J. Strangeway, R. Torbert, C. Hagen, I. Jernej, A. Valavanoglou, I. Richter, *Space Sci. Rev.* **199**(1), 189–256 (2016)
- J.A. Ryan, R.M. Henry, S.L. Hess, C.B. Leovy, J.E. Tillman, C. Walcek, *Geophys. Res. Lett.* **5**, 715–718 (1978)
- E.J. Smith, Planetary magnetic field experiments, in *Advanced Space Experiments*, ed. by O.L. Tiffany, E.M. Zaitzeff (American Astronautical Society, Tarzana, 1969), pp. 103–129
- S. Smrekar, P. Lognonné, T. Spohn, B. Banerdt, D. Breuer, U. Christensen, V. Dehant, M. Drilleau, B. Folkner, N. Fuji, R.F. Garcia, D. Giardini, M. Golombek, M. Grott, T. Gudkova, C. Johnson, A. Khan, B. Langlais, A. Mittelholz, A. Mocquet, B. Myhill, M. Panning, C. Perrin, T. Pike, A. Plesa, A. Rivoldini, H. Samuel, T. van Hoolst, O. Verhoeven, R. Weber, M. Wiczeorek, *Space Sci. Rev.* (2018). <https://doi.org/10.1007/s11214-018-0563-9>
- A. Spiga, D. Banfield, N.A. Teanby, F. Forget, A. Lucas, B. Kenda, J.A. Rodriguez Manfredi, R. Widmer-Schmidrig, N. Murdoch, M.T. Lemmon, R.F. Garcia, L. Martire, O. Karatekin, S. Le Maistre, B. Vam Hove, V. Dehant, P. Lognonné, N. Muller, R. Lorenz, D. Mimoun, S. Rodriguez, E. Beucler, I. Daubar, M.P. Golombek, T. Bertrand, Y. Nishikawa, S. Navarro, L. Mora-Sotomayor, E. Sebastian-Martinez, E. Millour, L. Rolland, Q. Brissaud, T. Kawamura, A. Mocquet, R. Martin, J. Clinton, E. Stutzmann, W.M. Folkner, J. Maki, T. Spohn, S. Smrekar, W.B. Banerdt, *Space Sci. Rev.* **214**(7), 1–64 (2018)

- J.M. Wilczak, A.J. Bedard, *J. Atmos. Ocean. Technol.* **21**, 1170–1181 (2004)
- J.-P. Williams, *J. Geophys. Res.* **106**(E3), 5033–5041 (2001). <https://doi.org/10.1029/1999JE001174>
- Y. Yeroshenko, W. Riedler, K. Schwingenschuh, J.G. Luhmann, M. Ong, C.T. Russell, *Geophys. Res. Lett.* **17**, 885–888 (1990)
- T.L. Zhang, W. Baumjohann, C.T. Russell, J.G. Luhmann, S.D. Xiao, *Sci. Rep.* **6**, 23537 (2016)
- M.-P. Zorzano, L. Vazquez, S. Jimenez, *Inverse Probl.* **25**, 115023–115032 (2009)
- W. Zürn, R. Widmer, *Geophys. Res. Lett.* **22**(24), 3537–3540 (1995)
- W. Zürn, J.H.S. Exß, C. Kroner, T. Jahr, M. Westerhaus, *Geophys. J. Int.* **171**, 780–796 (2007)